

## Marine Biology

July 2010, Volume 157, Number 7, Pages 1525-1541

<http://dx.doi.org/10.1007/s00227-010-1426-4>

© Springer-Verlag 2010

**Archimer**  
<http://archimer.ifremer.fr>

The original publication is available at <http://www.springerlink.com>

---

### **Predictive modelling of seabed habitats: case study of subtidal kelp forests on the coast of Brittany, France**

Vona Méléder<sup>1,3,\*</sup>, Jacques Populus<sup>1</sup>, Brigitte Guillaumont<sup>1</sup>, Thierry Perrot<sup>2</sup> and Pascal Mouquet<sup>2</sup>

<sup>1</sup> Ifremer, Dyneco/AG, BP 70, 29280 Plouzané, France

<sup>2</sup> CEVA, BP 3, L'Armor-Pleubian, 22610 Pleubian, France

<sup>3</sup> Present address: Nantes Atlantique Université, Mer Molécule Santé/EA 21 60, BP 92208, 44322 Nantes cedex 3, France

\*: Corresponding author : Vona Méléder, email address : [vona.meleder@univ-nantes.fr](mailto:vona.meleder@univ-nantes.fr)

---

#### **Abstract:**

Predictive modelling to map subtidal communities is an alternative to “traditional” methods, such as direct sampling, remote sensing and acoustic survey, which are neither time- nor cost-effective for vast expanses. The principle of this modelling is the use of a combination of environmental key parameters to produce rules to understand species distribution and hence generate predictive maps. This study focuses on subtidal kelp forests (KF) on the coast of Brittany, France. The most significant key parameters to predict KF frequency are (1) the nature of the substrate, (2) depth, (3) water transparency, (4) water surface temperature and (5) hydrodynamics associated with the flexibility of algae in a flow. All these parameters are integrated in a spatial model, built using a Geographical Information System. This model results in a KF frequency map, where sites with optimum key parameters show a deeper limit of disappearance. After validation, the model is used in the context of Climate Change to estimate the effect of environmental variation on this depth limit of KF. Thus, the effects of both an increase in water temperature and a decrease in its transparency could lead to the complete disappearance of KF.

## 38 INTRODUCTION

39 Traditionally, marine ecologists have used the direct sampling method to characterise  
40 shallow water and intertidal marine habitats. However, this method is neither time-  
41 nor cost effective for expanses from a regional to a global scale. Remote sensing  
42 tools, such as aerial photography, airborne and satellite imagery, are appropriate for  
43 surveying and classifying marine habitats in the intertidal zone (Guillaumont et al.  
44 1993; Bajjouk et al. 1996; Guillaumont et al. 1997; Méléder et al. 2003; Combe et al.  
45 2005). However, these tools rapidly reach their limits for subtidal surveys because of  
46 the absorption of visible radiations by water. Both single-beam and sidescan acoustic  
47 methods are suitable to overcome this limitation and to achieve remote sensing of  
48 depth and benthic communities in subtidal waters (McRea et al. 1999; Piazzini et al.  
49 2000; Brown et al. 2002; Freitas et al. 2003; Riegl et al. 2005; Freitas et al. 2006).  
50 But as these techniques involve either profiles or narrow swaths, their efficiency of  
51 coverage is quite limited and addressing areas from regional to global scale leads to  
52 dramatically increased costs. Acoustic methods also have limited discriminatory  
53 ability between macrophyte types and densities although recent works show their  
54 capability to coarse estimate macrophytic biomass (Riegl et al. 2005). So, for spatial  
55 assessment of seabed habitats, prediction using models seems to be the best  
56 approach. Depending of the objective of the survey and the availability of data to  
57 build models, assessment could include the occurrence, the biomass, the density  
58 and/or the diversity of habitats. Although these tools cannot replace direct detection  
59 or observation of benthic surfaces, they can provide a more global vision of some  
60 seabed habitats that is compatible with ecosystem management. The development of  
61 predictive models will contribute to better understanding of the factors and processes  
62 which structure the distribution and composition of marine habitats and their

63 associated biological communities at a coarser yet more integrated scale than that  
64 achieved using direct methods. Once developed and validated, these models are  
65 time- and cost-beneficial tools and enable the coverage of areas where no habitat  
66 information is available. Besides, they offer a way to apply scenarios to simulate  
67 effects of environmental changes on habitats distribution, particularly in the  
68 contemporary context of the Climate Change (IPCC 2001).

69 Some combinations of environmental parameters, such as the so-called the 'marine  
70 landscape', are assumed to control the distribution of species and habitat types (Roff  
71 and Taylor 2000). Basically, the key parameters used can be grouped under three  
72 themes (Stevens and Connolly 2004), i.e., those concerned with 1/ the morphology of  
73 the bottom and the nature of the substrate (depth, sediment type, sediment  
74 constituents), 2/ the nature of the water body overlying the substrate (temperature,  
75 pH, salinity, turbidity, nutrients) and 3/ the dynamics of the local environment or water  
76 mass (exposure to waves, current velocity). Since the approach proposed by Roff &  
77 Taylor in 2000 to predict the distribution of species and habitat types using 'marine  
78 landscapes', there have been a few examples of marine habitat classification in a  
79 spatial context based on physical factors (Zacharias et al. 1999; Kelly et al. 2001;  
80 Zacharias and Roff 2001; Brinkman et al. 2002; Stevens and Connolly 2004; Greve  
81 and Krause-Jensen 2005; De Oliveira et al. 2006). Applied to a marine context, these  
82 methodologies are expected to produce rules to understand species distribution  
83 according to environmental parameters and hence, predictive maps.

84 The aim of this study, part of a modelling work package of the MESH project  
85 (Mapping European Seabed Habitats), an Interreg IIIB North-West Europe funded  
86 initiative, is to propose a predictive model of kelp forest (hereafter called KF)

87 frequency, i.e., the percentage of their presence along the coast of Brittany, France.  
88 Indeed, seaweeds are an important component of coastal primary production. With a  
89 primary production ranging from 400 to 1900 g C.m<sup>-2</sup>.y<sup>-1</sup> (Sivertsen 1997), KF can be  
90 compared to the most productive terrestrial ecosystems (Hurd 2000). Characterised  
91 by densities of more than 3 plants.m<sup>-2</sup> and made up of various seaweed species  
92 belonging to the Laminariales order, essentially *Laminaria digitata* and *Laminaria*  
93 *hyperborean*, KF are often the dominant producers in nearshore ecosystems,  
94 supplying higher trophic levels via herbivory or the detrital food chain (Hurd 2000 and  
95 references within). KF also provide an essential habitat and food for hundreds of  
96 marine invertebrates and fish species living in temperate nearshore waters  
97 (Norderhaug et al. 2002 and references within). However, they also react to changes  
98 in environmental changes and/or quality (Dayton et al. 1992; Ferrat et al. 2003).  
99 Finally, KF are used in many maritime countries for industrial applications and as a  
100 fertiliser. This means that there is a steady demand for raw material from the  
101 seaweed industry, adding economic importance to their ecological one.

102 In this current study, KF frequency is predicted as a function of the depth and the  
103 chosen methodology for the prediction is the stepwise multiple regression process  
104 with a backward selection of environmental variables: water transparency,  
105 temperature and water motion. The software used to build and validate the model  
106 and to display the resulting map is a Geographical Information System (GIS), ArcGIS  
107 9.0. After validation, model is used in the context of Climate Change to estimate the  
108 effect of environmental variation on KF distribution.

109

110

111

## 112 MATERIALS AND METHODS

### 113 Environmental variables

114 *Nature of substrate* – As KF are mainly found on rocky substrata, the prediction of  
115 their occurrence was limited to this kind of substrate. Thus, maps of rock in shapefile  
116 format were used as masks to force the model in the GIS software, namely digital  
117 sediment maps (SHOM 1994-2005) with a resolution of 1:50,000 and where not  
118 available, a coarser 1:500,000 map (Vaslet et al. 1979).

119 *Bathymetry* – The bathymetry map was a raster dataset from the French Channel  
120 coast to the Gironde estuary, with a resolution of 150 m. This raster was generated  
121 using various types of digital and map depth data that were interpolated by kriging, a  
122 geostatistical method. Bathymetry was expressed in metres with respect to the LAT  
123 (lowest astronomical tide level). However, this depth did not correspond to the real  
124 water column height, since LAT levels are rarely reached. Therefore, depth values  
125 were locally corrected by the annual mean tide level, leading to a new raster dataset  
126 of water column height to be used as an input for the predictive model. For the sake  
127 of simplicity, this water height will be called “depth” in the paper.

128 Another bathymetric derivative was also calculated, the BPI (Bathymetric Position  
129 Index, Lundblad et al. 2004). This index enabled the topography to be estimated  
130 (crest / depression / flat or slope) by measuring where a given depth cell was located  
131 with regard to the overall landscape. In the present case the mean depth of the  
132 surrounding cells was computed using a 4 cell radius annulus. The cells in the  
133 resulting raster dataset were assigned values within a range of positive and negative  
134 numbers. A positive BPI indicated a cell on a crest, whereas a negative index was  
135 found where a depression occurred. Flats areas or areas with a constant slope  
136 produced index values near zero (Lundblad et al. 2004).

137 *Water transparency* – In coastal waters, light is very often a key limiting factor for the  
138 growth of photosynthetic organisms such as the laminarial algae constituting KF, and  
139 the light attenuation coefficient in the euphotic layer is a major parameter used in  
140 ecological modelling. Thus, the attenuation coefficient of the photosynthetically  
141 available radiation (PAR domain [400 – 700 nm]),  $K_{PAR}$  enabled the light attenuation  
142 throughout the water column to be modelled. This coefficient, derived from the water  
143 optically active components related to chlorophyll, suspended particulate matter and  
144 dissolved organic matter could be used as a water turbidity proxy. Hence, a high  
145 attenuation coefficient illustrates a turbid water column. In this study,  $K_{PAR}$  was  
146 derived from SeaWiFS (Sea Wide Field Sensor) satellite reflectance, combining  
147 chlorophyll and suspended matter optical properties (Gohin et al. 2005). 52 weekly  
148 mean images of  $K_{PAR}$  were obtained from SeaWiFS data averaged over the 1998-  
149 2004 period, with a resolution of 1,100 m.

150 From this  $K_{PAR}$  the fraction of light reaching the bottom ( $Fr$ ) was estimated for a given  
151 depth  $h$  by:

$$152 \quad Fr = (\exp^{-h \times K_{PAR}}) \times 100 \quad (\%) \quad (1)$$

153 When this percentage is equal to 1%, it defines the lower limit of the photic zone.

154 Below this threshold, the remaining energy is not efficient for photosynthesis.

155 *Temperature* – This factor was estimated by Sea Surface Temperature (SST, in °C)

156 derived from AVHRR (Advanced Very High Resolution Radiometer) data with a

157 resolution of 1,100 m. SST maps were provided by the SAF (Satellite Application

158 Facility) “Ocean and Sea Ice” of EUMETSTAT/Meteo-France, Lannion (France) and

159 52 weekly mean images were available from AVHRR reflectance averaged over the

160 last two decades.

161 *Water motion* – This variable was expressed as the tidal current maximum velocity  
162 ( $V_{max}$  in  $m.s^{-1}$ ) resulting from simulations for a mean spring tide run by the  
163 hydrodynamic model MARS 3D developed at Ifremer. The current resolution of this  
164 model is 300 m.

165

166 Biological variables: KF ground-truthing

167 Acoustic surveys of laminarial algae belonging to KF were carried out at 10 locations  
168 along the Coast of Brittany in three periods: spring 2005 for the Aber Wrac'h (AW)  
169 site, spring 2006 for the Groix (Gr), Molène (Mo), Méloine (Me) and Triagoz (Tr) sites  
170 and spring 2007 for the Audierne (Au), Bréhat Island (Br), Glénan (Gl), Heaux (He)  
171 and Moelan (MI) sites (Figure 1). All sites were chosen for the presence of rocky  
172 substrata and the accessibility to survey boat. Prospected zone for each site was  
173 delimited using rock and bathymetry maps to identify flat rocky area located at a  
174 bathymetry varying from 10 to 30 m, where KF were more susceptible to be found.  
175 On field, a small survey boat equipped with a 120 kHz Simrad EK60 echo-sounder  
176 was used. The narrow 7° width beams were used for emitting and receiving. The  
177 acquisition parameters of the transducer, adjusted to the minimum pulse duration (64  
178 μs) and sampling interval (pulse frequency: 16 μs), made it possible to obtain the  
179 maximum resolution on both vertical and horizontal axes. All recordings were  
180 performed at a constant speed of about 5 knots corresponding to a distance between  
181 each pulse (or ping) varying from 5 to 20 cm. The total track length for each site was  
182 about 20 kilometres. Acoustic transects were simultaneously georeferenced with a  
183 GPS equipped with the EGNOS system giving position accuracy of better than three  
184 metres. Both acoustic and position data were stored on a laptop PC.

185 *Data processing* - Raw acoustic data were post-processed using MOVIES+ echo  
186 integration software (Marchalot et al. 2003) which can be used to evaluate the  
187 backscattered energy in different depth layers defined by the user above or below the  
188 seafloor (Figure 2, line A). The first layer was defined at 0.2 m above the sea bottom  
189 to detected KF (Figure 2, line B) and the second from 1 to 1.5 m under the sea  
190 bottom to evaluate the nature of the seafloor (not shown in Figure 2). The top limit of  
191 the integrated layer was set at 2.2 m above the bottom (line C). On each ESU  
192 (Elementary Sampling Unit, Figure 2), defined by a 20-ping width and a spatial  
193 resolution varying from 1 to 4 m (depending on the speed of the boat), the software  
194 gives four parameters for each layer:  $N_i$  (number of echo-integrated samples),  $N_t$   
195 (total number of samples),  $sA$  (nautical area scattering coefficient in the layer in  
196  $m^2/mille^2$ ) and  $sV$  (volume reverberation index of the layer in dB). The additional  
197 parameter *BotErr* (for Bottom Error), provided by the software when a large variation  
198 is detected in the echo-integrated energy, may indicate that the bottom itself has  
199 accidentally been integrated in the first bottom layer (i.e., the one nearest the sea  
200 bed, see Figure 2, line A). Once the raw acoustic data have been processed using  
201 MOVIES+, a specific algorithm implemented with the Excel software based on  
202 thresholds and ratio values of  $N_i$ ,  $N_t$ ,  $sA$  and *BotErr* automatically classifies KF  
203 presence or absence (binary) and the type of substrate (rock or sand). The algorithm  
204 was validated using direct observations by scuba-divers on the AW site during spring  
205 2005 and in the Gr, Mo, Me and Tr sites during the spring 2006.

206 Thus, the resulting data for each ESU were the coordinates of the point (lat, long),  
207 the KF presence or absence, the nature of the substratum, and the depth (in metres).  
208 The latter, initially measured with reference to LAT, was corrected by adding the  
209 annual mean tide level.

210 The echo-integration results were used to build KF distribution laws, expressed for  
 211 each site in “percentage of presence” or “frequency” (%) as a function of depth (m).

212 KF frequency,  $F_{[H]}$ , was obtained for depths between 10 and 30 m by:

$$213 \quad F_{[H]} = \frac{\sum_{h < H+0.25} KF_H}{\sum_{h \geq H-0.25} R_H} \times 100 \quad (2)$$

214 where H was the class of depth split into 0.5 m intervals and  $h$  the depth from echo-  
 215 integration falling into this class,  $KF_H$  the total amount of ESU corresponding to KF for  
 216 the given class H and  $R_H$  the total amount of ESU corresponding to rock substratum  
 217 for the same class H.

218 These frequency laws were fitted using piecewise regressions (Toms and  
 219 Lesperance 2003) from SigmaPlot 10.0 software following the process:

$$220 \quad h_1 = \min(h)$$

$$221 \quad h_3 = \max(h)$$

$$222 \quad \text{segment1}(h) = (y_1 \times (H_1 - h) + y_2 \times (h - H_1)) / (H_1 - h_1) \quad (3)$$

$$223 \quad \text{segment2}(h) = (y_2 \times (H_2 - h) + y_3 \times (h - H_1)) / (H_2 - H_1) \quad (4)$$

$$224 \quad \text{segment3}(h) = (y_3 \times (h_3 - h) + y_4 \times (h - H_2)) / (h_3 - H_2) \quad (5)$$

$$225 \quad f = \text{if } (h \leq H_1 ; \text{segment1}(h) ; \text{if } (h \leq H_2 ; \text{segment2}(h) ; \text{segment3}(h))$$

226

227 The fit was sought for the two breakpoints  $H_1$  and  $H_2$  and  $\text{Slope}_2$ , the slope between  
 228 them (Figure 3).  $H_1$  and  $H_2$  were the depths corresponding respectively to the  
 229 beginning of the frequency decrease and to the disappearance of KF, (which is also  
 230 the upper limit of KF characterised by a density of less than 3 plants.m<sup>-2</sup>). These  
 231 three parameters were taken as the biological variables to be predicted using

232 environmental ones. Each fit was expressed with its confidence and prediction  
233 intervals at 95 % (Figure 3).

234

235 Model building

236 The cell values of the environmental variable raster dataset (BPI,  $K_{PAR}$ , SST and  
237  $V_{max}$ ) intersected by acoustically surveyed transects were extracted and averaged  
238 on a site basis. The values from five sites (AW, Mo, Me, Tr and Gr) called “training  
239 sites” were used to build the predictive model of KF frequency, whereas the values  
240 from the other five (Au, Br, Gl, He and MI called “validation sites”) were used to  
241 validate it.

242 The methodology chosen for the prediction was the stepwise multiple regression with  
243 a backward selection of variables. Associations of the BPI and/or  $K_{PAR}$  and/or SST  
244 and/or  $V_{max}$  were used to predict  $H_1$ ,  $H_2$  and  $Slope_2$ , and then to estimate KF  
245 frequency for depths from  $H_1$  to  $H_2$ :

$$246 \quad H_1 = aBPI + bSST + cK_{PAR} + dV_{max}^{\beta} \quad (6)$$

$$247 \quad H_2 = a'BPI + b'SST + c'K_{PAR} + d'V_{max}^{\beta} \quad (7)$$

$$248 \quad Slope_2 = a''BPI + b''SST + c''K_{PAR} + d''V_{max}^{\beta} \quad (8)$$

$$249 \quad \text{Predicted KF frequency (\%)} = Slope_2 \times (h - H_2) \quad \text{for } H_1 < h < H_2 \quad (9)$$

250 where, a to c'' were the regression coefficients (might be = 0), and the  $\beta$  exponent  
251 expressed the flexibility of algae in a flow, typically around 1.5 (Denny and Gaylord  
252 2002). 2 and 1.5 were tested as values for  $\beta$ .

253

254 The prediction of KF frequency for a depth less than  $H_1$  is performed using the same  
255 process:

$$256 \quad \text{Predicted KF frequency (\%)} = wBPI + xSST + yK_{PAR} + zV_{max}^{\beta} \quad (10)$$

257           for  $h < H_1$   
258   where  $w$  to  $z$  are the regression coefficients (might be = 0) and  $\beta=1.5$  or 2.  
259  
260   Stepwise regressions were run using the statistical software R.2.5.1. However, the  
261   use in regression process of the 52 weekly values extracted from  $K_{PAR}$  and SST  
262   images was not relevant. For this reason, water transparency and surface  
263   temperature information were synthesised using both the annual average (namely  
264    $K_{PARyear}$  and  $SSTyear$ ) and the average during the growth period from week 14 to  
265   week 25 (namely  $K_{PARgrowth}$  and  $SSTgrowth$ ). The minimum and maximum values  
266   during the year ( $K_{PARmin}$ ,  $SSTmin$ ,  $K_{PARmax}$  and  $SSTmax$ ) were also integrated in  
267   the stepwise regression process. Then environmental variables with a non-significant  
268   partial F ( $p \leq 0.1$ ) were removed step by step. However, varying significant multiple  
269   or simple regressions were obtained to predict the same biological variables. All  
270   these regressions were used to build varying predictive models, and the one showing  
271   the smallest residual differences between predictions and observations was kept to  
272   produce the final predictive map. This map was then built by automating the model  
273   work flow with the 'ModelBuilder' interface in the ArcGIS 9.0 geoprocessing toolbox.  
274   Moreover, this interface allowed to create the environmental settings for the model,  
275   which controlled geoprocessing output parameters. Raster analysis settings were  
276   used to give the output cell size, defining working scale, the finest resolution among  
277   the various data sources, 150 m, and to apply the rock mask.

278

279   Validation and simulations

280   KF frequency obtained by echo-sounding from the 5 sites: Au, Br, Gl, He and Mo

281   (Figure 1) was compared to the prediction at the same location to validate the model.

282 It was then used in the context of Climate Change to estimate the effect of  
283 environmental variation on the depth of KF disappearance,  $H_2$ . Indeed, since 1976,  
284 temperature of the ocean increase by 0.075 °C/decade, i.e. an increase of around  
285 0.2 °C during the 30 past years (IPCC 2001). For the northern hemisphere, where  
286 this study sites are located, the increase of temperature is higher with 0.4 °C/decade,  
287 i.e. around 1 °C since 1976 (IPCC 2001). Using the validated model, two scenarii  
288 were tested for temperature increase in accordance to IPCC (2001) results: the  
289 global (0.2 °C) and the northern increase (1 °C). An intermediate stage (an increase  
290 of 0.5 °C) was used in a third simulation. In the same way, three scenarii to estimate  
291 effect of an increase of water transparency on KF distribution were tested. Indeed,  
292 extreme episodic events such as storms, extreme rain events and flooding must a  
293 consequence of the Climate Change (IPCC 2001). These result in strong  
294 hydrodynamics and super river discharges leading to decrease of water transparency  
295 (de Jonge and de Jong 2002; Cardoso et al. 2008). However, no information about  
296 the evolution of the water transparency proxy use in this study, the  $K_{PAR}$ , is available.  
297 Steps to simulate increase of  $K_{PAR}$  values for the three scenarii were chosen to test  
298  $K_{PAR}$  values included in the range of values used to build the model: 0.01, 0.02 and  
299 0.05.

300

## 301 RESULTS

### 302 Environmental parameters

303 Gr, He and Br sites were the more turbid locations throughout the year and during  
304 the growth period with the greatest  $K_{PARyear}$  and  $K_{PARgrowth}$  values (Table 1). For  
305 these three sites, the minimum values ( $K_{PARmin}$ ) never went below 0.18, whereas  
306 maximum values ( $K_{PARmax}$ ) reached 0.456 at the Gr site during week 2 (Table 1,

307 Figure 4). On the other hand, the western sites Mo and Au were the clearest  
308 locations with lowest  $K_{PAR}$  values (Table 1).  
309 Along with this spatial variability along the coast of Brittany, water transparency also  
310 varied over time. Peaks of  $K_{PAR}$ , often exceeding 0.25, were detected during the first  
311 seven weeks and the last twelve weeks (Figure 4). These periods corresponded  
312 respectively to winter and autumn, periods of bad weather with rain and storms often  
313 leading to increased amounts of mineral material from either bottom scouring or river  
314 discharge. The maximum  $K_{PAR}$  values reported in Table 1 were recorded during  
315 these weeks. Conversely, the minimum  $K_{PAR}$  values ( $K_{PARmin}$ , Table 1) were  
316 observed during spring/summer between weeks 10 and 40. This period  
317 corresponded to calm weather, although some turbulent and stochastic events  
318 appeared and generated turbidity peaks lasting from one to three weeks but never  
319 resulting in a  $K_{PAR}$  above 0.25 (Figure 4). These peaks were essentially observed at  
320 AW, Gr, Br and He sites, whereas the other sites were more stable in terms of water  
321 transparency (Figure 4).

322

323 Surface temperature showed spatial and temporal variability very similar to that of  
324 water transparency. The warmest sites during the year were those located in the  
325 south: Gr, Gl and Ml with respectively 13.6, 13.7 and 13.5°C (Table 1), which also  
326 exhibited growth period temperature values in excess of 12.5°C. The coldest site  
327 was AW with more than 1°C below the annual means of the southern sites. The  
328 other sites showed equivalent annual SST values, around 13°C (Table 1).

329 The temporal variability was classic, with high temperatures in summer, and low  
330 temperatures in winter (Figure 5). However the Gr site, although it was one of the  
331 warmest, showed the minimum temperature value (8.7° C), due to a well-known

332 tongue of cold water occurring near the coast. The other southern sites showed the  
333 highest minimum and maximum temperature values (Table 1, Figure 5).

334

335 Exposure, measured by the maximum tidal current velocity  $V_{max}$ , showed a  
336 north/south gradient whose maximum velocity was lower than  $0.3 \text{ m.s}^{-1}$  for southern  
337 sites, although it reached  $1 \text{ m.s}^{-1}$  for the more turbulent northern sites (Table 1).

338

339 Surveying KF with echo-sounding

340 The parameters described in the Materials and Methods section were calculated for  
341 the echo signals collected over the study areas and the binary classification of KF  
342 (presence/absence) was performed for each site. For illustrate results, only part of  
343 the echogram for the GI site and the corresponding classification are shown in Figure  
344 6. The acoustic signal from KF is about 1 metre high with quite low backscatter  
345 energy (light grey) above the seafloor (dark grey). There was good correlation  
346 between underwater KF boundaries as indicated by the echogram and the  
347 classification (dark hatches). Sometimes, accidental bottom integration causes  
348 classification of the ESU in *BottErr* (light hatches). This phenomenon is generally  
349 seen on steeper rocky substrates and is amplified by bad weather conditions.

350

351 KF frequency law

352 Overall, the sites showed the same significant distribution profile along the depth  
353 (Figure 3, Table 2), except for those of Au, He and MI, for which some fit parameters  
354 are not significant (Table 2). The profile was divided in two parts. The first, before the  
355 inflexion point  $H_1$ , corresponded to the variability of frequency around a mean (Figure  
356 3). The slope of this first segment was not significant, and thus, was not predicted by

357 the model. Indeed, the frequency for depths less than  $H_1$  up to the upper KF limit  
358 were directly predicted using environmental parameters (eq. 10). The second part of  
359 distribution law corresponded to a drop in the frequency along Slope<sub>2</sub>, between  $H_1$ ,  
360 and  $H_2$ , the depth at which KF disappeared (eq. 4 to 6). Fits are good, with high  
361 adjusted  $R^2$  and a probability of less than 0.01 (Table 2).  $H_1$  varies from 13.2 m for  
362 the most turbid and coldest site Br, to 20.6 m for the clearest and warmest one, Mo  
363 (Tables 1 and 2). Likewise, Slope<sub>2</sub> is higher in turbid (low transparency) and cold  
364 sites, such as Au and Br, than in less turbid and warmer sites such as Me and AW  
365 (Tables 1 and 2). Similarly to  $H_1$  and Slope<sub>2</sub>,  $H_2$  varies with the water transparency  
366 and surface temperature from 19.3 m to 27.8 m. However, the relationship between  
367  $H_2$  and water transparency and/or surface temperature is not as clear as that  
368 explaining  $H_1$  and Slope<sub>2</sub>, suggesting the effect of another environmental parameter  
369 to explain explaining KF disappearance, which could be bed stress.

370 Once  $H_2$  was known, the Fr fraction (eq. 1) for each site was calculated using the  
371 four water transparency parameters  $K_{PARyear}$ ,  $K_{PARgrowth}$ ,  $K_{PARmin}$  and  $K_{PARmax}$   
372 (Table 3). Only  $K_{PARgrowth}$  and  $K_{PARmin}$  values allowed Fr higher than the 1%  
373 threshold permitting photosynthesis activity. The use of  $K_{PARyear}$  and  $K_{PARmax}$   
374 generated Fr values below the 1% level which were inconsistent with algal presence  
375 such as KF or parks. Thus, only  $K_{PARgrowth}$  and  $K_{PARmin}$  seemed to be relevant and  
376 biologically interpretable abiotic factors to predict  $H_2$  and hence KF frequency.

377

## 378 Predictive modelling

379 Stepwise regression processes provided four significant models to predict KF  
380 frequency from the five training sites AW, Mo, Me, Tr and Gr, for a depth ranging  
381 from  $H_1$  to  $H_2$  following the equations (6) to (9). The first model predicted biological

382 variables ( $H_1$ ,  $H_2$  and  $Slope_2$ ) using SSTmin only (eqs. 11 to 13) and the second one  
 383 used  $K_{PARmin}$  only (eqs. 14 to 16). The last two significant models were similar to the  
 384 first two, but with a better predictive  $H_2$  using  $Vmax^{1.5}$  in addition to SSTmin or  
 385  $K_{PARmin}$  alone (eqs. 17 and 18). The adjusted  $R^2$  increased from 0.80 to 0.98 when  
 386  $Vmax^{1.5}$  was associated with SSTmin, and from 0.76 to 0.97 when  $Vmax^{1.5}$  was  
 387 associated with  $K_{PARmin}$ :

388

389 pred\_mod1,

390  $H_1 = - 29.81 + 5.31 \times SSTmin$   $R^2 = 0.88, p \leq 0.05$  (11)

391  $H_2 = - 30.32 + 5.86 \times SSTmin$   $R^2 = 0.80, p \leq 0.05$  (12)

392  $Slope_2 = 28.53 - 4.23 \times SSTmin$   $R^2 = 0.79, p \leq 0.05$  (13)

393 pred\_mod2,

394  $H_1 = 40.5 - 121.19 \times K_{PARmin}$   $R^2 = 0.87, p \leq 0.05$  (14)

395  $H_2 = 40.75 - 130.97 \times K_{PARmin}$   $R^2 = 0.76, p \leq 0.05$  (15)

396  $Slope_2 = - 25.37 + 84.72 \times K_{PARmin}$   $R^2 = 0.60, p = 0.12$  (16)

397 pred\_mod3,

398  $H_1 = \text{eq. (14)}$

399  $H_2 = 43.53 - 121.12 \times K_{PARmin} + 2.26 \times Vmax^{1.5}$   $R^2 = 0.97, p \leq 0.05$  (17)

400  $Slope_2 = \text{eq. (16)}$

401 pred\_mod4,

402  $H_1 = \text{eq. (11)}$

403  $H_2 = - 26.86 + 5.33 \times SSTmin + 2.07 \times Vmax^{1.5}$   $R^2 = 0.98, p \leq 0.05$  (18)

404                    Slope<sub>2</sub>= eq. (13)

405    For each model, the KF frequency was predicted following equation (9). Thus, the  
406    most efficient model was that reducing residuals between observation and prediction  
407    (Figure 7). These residuals showed that models including temperature or water  
408    transparency only (respectively pred\_mod1 and pred\_mod2) were not able to predict  
409    KF frequency correctly (Figure 7a and 7b). Indeed, SSTmin on its own (pred\_mod1)  
410    predicted KF frequency well only for the Gr and Me sites, whereas this model  
411    overestimated percentages for the sites AW and Mo and underestimated them for Tr  
412    (Figure 7a). On the contrary, K<sub>PAR</sub>min (pred\_mod2, Figure 7b) enabled good  
413    prediction for the latter site as well as for Me, while it overestimated observations for  
414    Mo and underestimated those on AW. The use of water motion, estimating bed  
415    stress using Vmax<sup>1.5</sup>, was more efficient (Figure 7c and 7d) particularly when it was  
416    associated with water transparency (Figure 7c). Only the observed frequencies from  
417    the Gr site were not well predicted using the model 'pred\_mod3' but this was due to  
418    incomplete coverage by SeaWiFS data for this site. Therefore, the model using  
419    SSTmin and Vmax<sup>1.5</sup> (Figure 7d) was run for part of this site and other locations  
420    where water transparency data were not available.

421    Models were able thus to predict a decrease in depths H<sub>1</sub> and H<sub>2</sub> with water clarity,  
422    while an increase in temperature indicated deeper breakpoints. When clearness or  
423    surface temperature of water was constant a drop in the depth limit H<sub>2</sub> occurred in a  
424    direct ratio with a power of 1.5 for the velocity. Finally, the model providing the best  
425    prediction of KF frequency for depths between H<sub>1</sub> to H<sub>2</sub> was pred\_mod3, using water  
426    transparency and bed stress, or pred\_mod4 when water transparency data were not  
427    available.

428

429 However, the only significant model to predict KF frequency for a depth less than  $H_1$ ,  
430 following equation (10) was that using topography (BPI) alone:

431 
$$\text{Predict \%} = 52.5 - 1.64 \times \text{BPI} \qquad R^2 = 0.75, p \leq 0.01 \text{ (19)}$$

432

433 This regression indicates that KF were observed preferentially in depressions rather  
434 than on crests. But, the attempted validation of this model concluded that using BPI  
435 as a physical parameter can correctly predict KF frequency values around 50%  
436 (Figure 8). Under or above this frequency, BPI alone did not explain occurrences of  
437 KF in well-lit water.

438 The prediction was stopped at the +1m depth contour, known to be the higher limit of  
439 KF presence. It was not possible to predict this limit at the study scale, as was done  
440 by De Oliveira (2006) who used the percentage of immersion over the year, derived  
441 from the tidal flooding frequency at a given elevation. This limit occurred for KF  
442 between immersion periods ranging from 92 to 97 % whereas maximum KF  
443 coverage occurred at 100 % immersion. The depth contours corresponding to ~ 95 %  
444 and 100 % immersion were too close (only a few tens of metres), so they were  
445 included in the same pixels of the bathymetry dataset used in our model. Therefore,  
446 estimating and mapping the decrease in KF frequency between these two contours  
447 at our working scale (150 m) was not possible.

448 Model validation

449 Validation sites Au, Br, Gl, He and MI (Figure 1) were used to validate the selected  
450 model providing the better prediction, by looking at the residuals between the KF  
451 frequency obtained by echo-sounding and predicted KF (Figure 9a). The prediction of

452 KF frequency between  $H_1$  and  $H_2$  is satisfactory for Au and GI sites but not as good  
453 for He, Br and MI sites, for which some KF frequency predictions overestimated the  
454 observations (Figure 9a).

455 For depths of less than  $H_1$ , the model using BPI alone is not too effective (Figure 9b).  
456 Observed frequencies varied from 10 to 64 % for all the sites, whereas predictions  
457 varied from 40 to 55 %. This indicates a limitation of the predictive model using only  
458 BPI for depths less than  $H_1$ .

459 In spite of these limits, the model provided good prediction of the boundary of KF  
460 disappearance  $H_2$ , on validation sites as well as on training sites (Table 4).

461

462 Predictive map

463 A predictive map is proposed to visualise areas where KF may occur as driven by  
464 environmental parameters (Figure 10). Three examples were taken to illustrate this  
465 map, AW, Br and GI sites, respectively shown by black, red and blue boxes (Figure  
466 10). AW is one of the sites showing highest hydrodynamism with great  $V_{max}$  and  $K_{PAR}$   
467 values, whereas GI is one of the less agitated sites and Br shows an intermediate  
468 stage.

469 KF disappear at greater depth when the water column is clear and not too cold. This  
470 is the case for the site AW site (black box, Figure 10). On this site, KF regularly  
471 reaches the 30 m depth contour. For more turbid and colder sites such as Br, KF only  
472 reaches the 20 m contour (red box, Figure 10). Exposure is also responsible for the  
473 decrease in the KF depth limit. For example, although the GI site is clearer than AW,  
474 KF there do not reach the 30 m contour, or only very locally (blue box, Figure 10).  
475 This is explained by the lower maximum velocity at GI than at AW (Table 1).

476

477 Simulation

478 In the context of Climate Change, the model was used to predict the potential  
479 variation in the KF disappearance depth,  $H_2$ , with respect to various scenarios.  
480 Simulations were based on an increase in  $K_{PARmin}$  of 0.01, 0.02 and 0.05, except for  
481 locations where no turbidity data were available. For the latter,  $SST_{min}$  was used  
482 with an increase of 0.2, 0.5 and 1°C. The results illustrated the antagonism of these  
483 two environmental parameters: an increase in water transparency induced an upward  
484 shift of the KF boundary while temperature was responsible for a downward one  
485 (Table 4). On sites AW, Me, Mo, Tr, Br, Gl and He (where  $K_{PARmin}$  was used),  $H_2$   
486 decreases of 1.2 m, 1.3 m and 3.6 m were obtained with  $K_{PARmin}$  respectively  
487 increasing by 0.01, 0.02 and 0.05 (Table 4). On the other hand, on sites for which  
488  $SST_{min}$  was used (Gr, Au and MI),  $H_2$  rose by 1, 2.5 and 5.5 m when SST  
489 respectively increased by 0.2, 0.5 and 1°C (Table 4).

490

## 491 DISCUSSION

492 *Environmental effect – Antagonism between water transparency and water*  
493 *temperature.*

494 Water transparency and water temperature are the two main environmental variables  
495 structuring KF frequency and distribution over the coast of Brittany. The results of this  
496 study conclude that the annual minimum value of the light attenuation coefficient by  
497 the water column is the most significant and relevant water transparency proxy for KF  
498 prediction. This minimum value is measured during spring/summer, corresponding to  
499 calm weather and thus to high water transparency because of limited sediment  
500 scouring from the bottom and river discharges. It is also during this period that  
501 maximum photosynthesis activity occurs, and the literature bears out that light

502 attenuation by the water column is a key parameter in the structuring of macroalgae  
503 communities, essentially during spring/summer (Belsher 1986; Markager and Sand-  
504 Jensen 1992) because of this maximum photosynthesis activity. This period of the  
505 year is favourable to KF growth all the more so nutrients are not limiting factors in  
506 Brittany costal water (Ménesguen et al. 1997). This also explains why the value of  
507 the light attenuation coefficient measured during the few weeks defining the growth  
508 period is another relevant water transparency proxy for KF prediction. This is  
509 supported by calculating the percentage of incident light lightening the limit of KF  
510 disappearance. According to Markager and Send-Jensen (1992) and references  
511 within showing the percentage of incidental light ranging from 0.7 to 1.9 % reaching  
512 the depth limit for *Laminaria hyperborea*, both minimum and growth values of  $K_{PAR}$   
513 are responsible for a percentage which is often higher than the 1% threshold  
514 permitting photosynthesis. Then, below the KF depth limit, the remaining light energy  
515 could be used by other photoautotrophic communities or organisms. KF are replaced  
516 by less dense communities, such as laminarial parks characterised by a density of  
517 less than 3 plants.m<sup>-2</sup>, and shade-loving species belonging to the Rhodophyceae  
518 class like *Solieria chordalis*.

519

520 Using water transparency to predict the KF depth limit is also an interesting approach  
521 in the context of Climate Change. Climate changes, including higher temperatures,  
522 precipitation and wind speeds as well as storm events, may increase the risk of  
523 abrupt and non-linear changes in many ecosystems, which would affect their  
524 composition, function, biodiversity and productivity (IPCC 2001). Episodic events  
525 such as storms, extreme rain events and flooding resulting in strong hydrodynamics  
526 and super river discharges can lead to increased amounts of suspended mineral

527 matter in the water column and on the bottom substrate (de Jonge and de Jong  
528 2002; Cardoso et al. 2008). This turbidity increase is reinforced by anthropogenic  
529 activities responsible for multiple stressors including pollutants, excess nutrients,  
530 altered habitats and hydrological regimes as well as floods and droughts (Cardoso et  
531 al. 2008). The response of KF to this drop in water transparency is bound to be an  
532 upward shift of their lower limit.

533 Nevertheless, the KF depth limit shift due to natural or anthropogenic turbidity  
534 increases could be counterbalanced by a rise in water temperature. Indeed, this  
535 study concludes that KF take advantage of temperature increases, with communities  
536 spreading towards deeper levels. The use of water temperature for prediction is more  
537 relevant when values are measured outside of the summer period. During these  
538 warm months, water column stratification can occur and therefore surface  
539 temperature is not a good proxy for bottom temperature. The rest of the year, when  
540 the water column is fairly homogenous and the bottom water is slightly cooler than at  
541 the surface, surface temperature is a good proxy for the entire column. Next, one of  
542 the structuring factors of Brittany KF communities is a minimum value of surface  
543 temperature measured during winter, varying from 8.3 to 9.6 °C. These low  
544 temperatures are without consequences for *Laminaria digitata*, the major species  
545 providing high KF levels (approximately from the LAT down to a depth of 5 m), as  
546 their broad ecological optimum varies from 3 to 15 °C (Belsher 1986). On the other  
547 hand, *L. hyperborea*, the major species making up the lower-lying part of KF  
548 (approximately from LAT to the depth limit) is more sensitive to cold temperature. Its  
549 optimum is narrower than that of *L. digitata*, varying from 10 to 17 °C and young  
550 sporophyte growth is altered at temperatures less than 10 °C (Belsher 1986). This  
551 explains why a rise in colder temperatures favours the spreading of these

552 communities towards deeper levels. Using temperature measured during the cold  
553 period for predictions is also an interesting approach in the case of Climate Change,  
554 because water warming is mainly observed during this period (Koutsikopoulos et al.  
555 1998). Nevertheless, although an increase in the coldest temperatures, as a  
556 consequence of Climate Change, seems to favour a downward KF shift, this  
557 phenomenon could be moderated or even reversed by the decrease in water  
558 transparency during calm periods. These two parameters have an antagonistic effect  
559 on KF structure.

560 Moreover, although the current model was not able to predict an effect on KF upper  
561 limits, the temperature increase observed over the past decades (IPCC 2001) could  
562 have a harmful effect on them. Indeed, *L. digitata* which occupies the upper part of  
563 KF, shows an optimum until 15°C, and a lethal temperature value around 23 - 24 °C  
564 (Belsher 1986). The latter values have not been observed along the coast of Brittany  
565 using the AVHRR scale, but, if surface temperatures kept increasing (as could be the  
566 case locally), lethal values would soon be reached. This warming effect would lead to  
567 KF reaching deeper and cooler water.

568 Then, in the worse Climate Change scenario, showing a rapid, high rise in  
569 temperature with an increase in the number and intensity of extreme events (IPCC,  
570 2001), the consequences will be an upward shift of the depth limit and a downward  
571 one of the upper KF boundary, leading to a reduction in their width. If worse comes to  
572 worst, the effects of both an increase in water temperature and a decrease in  
573 transparency could lead to the complete disappearance of KF. This dramatic  
574 consequence would lower or eliminate the habitat surface area and alter the  
575 diversity, abundance and functioning of the associated biological communities. This  
576 depletion of the ecosystem will also have economic consequences because of the

577 decrease of this resource already threatened by over-cropping (MEDD 2005). All  
578 these consequences will be irremediable if no global resolution like that  
579 recommended by the Intergovernmental Panel on Climate Change (IPCC,  
580 <http://www.ipcc.ch>) is adopted in the next few years.

581

582 *Environment effect – Bed stress issue*

583 Although the main studies assessing macro-algae with regard to exposure involve  
584 wave swell effects and the intertidal area (Denny 1995; Hurd 2000; Denny and  
585 Gaylord 2002; Buck and Buchholz 2005; Boller and Carrington 2006), this study  
586 considered exposure due to tidal currents. Numerous authors have shown the effect  
587 of orbital wave velocity, responsible for a drag force tending to push an object  
588 downstream, which depends on the water density and velocity exponent of drag,  $\beta$   
589 (Denny 1995). This exponent is derived from Vogel's  $E$  (Vogel 1994), and measures  
590 the relationship between velocity and drag. It determines how force increases with an  
591 increase in water velocity. For bluff objects subjected to drag,  $\beta$  is approximately 2  
592 (Denny 1995; Denny and Gaylord 2002) and numerous authors take this value for all  
593 objects, whether flexible or not (Buck and Buchholz 2005; Boller and Carrington  
594 2006; Pope et al. 2006). However, Vogel (1994) and Denny (1995) suggest that an  
595 exponent value lesser than 2 be used for streamlined or flexible objects. Indeed, in a  
596 unidirectional flow, algal fronds bend in response to the force applied, and the plant  
597 reorients and rearranges itself passively in a way resulting in overall streamlining  
598 (Denny 1995 and references within). Consequently, the  $\beta$  for exposed algae in flow is  
599 universally less than 2 and typically around 1.5 (Denny 1995), with the velocity-  
600 dependant character of shape being incorporated in this exponent. In this study,  
601 because of the lack of swell data for the entire survey area at an appropriate scale,

602 the effect of tidal current velocity was tested as a proxy for global water motion. The  
603 results confirm Denny's suggestion: the value 1.5 for velocity exponent of drag is  
604 more significant than the value 2, although water velocity does not have the same  
605 source (swell vs. tide). The effect of a velocity increase is positive for KF: for sites  
606 with the same water transparency conditions, a velocity greater than  $0.8 \text{ m}\cdot\text{s}^{-1}$   
607 induces a downward shift of KF depth limit. This could be explained by a regular  
608 cleaning effect of thalli in wild sites, making them more receptive to  
609 photosynthetically available radiation than in sheltered sites where thalli are often  
610 covered with a thin layer of particles. On the other hand, and although this has not  
611 been observed on the scale and the sites of this study, too high a velocity is not  
612 beneficial for KF, which could be dislodged or destroyed, as shown *in situ* or  
613 experimentally for a number of macroalgae species (Gaylord et al. 2003; Buck and  
614 Buchholz 2005; Boller and Carrington 2006). Indeed, the shear stress imposed on a  
615 structure by water velocity of  $2 \text{ m}\cdot\text{s}^{-1}$  is roughly equivalent to that exerted by wind of  
616  $130 \text{ miles}\cdot\text{h}^{-1}$  (Denny and Gaylord 2002).

617 Another proxy for exposure is the topography. This environmental variable is the only  
618 one explaining KF structures when water temperature and transparency are not  
619 limiting factors, that is to say in shallow depths. KF are observed more often, on a  
620 working scale, in depressions rather than on crests. This could be explained by the  
621 fact that crests are too exposed to the swell and tidal currents and therefore KF  
622 would be overly subjected to high drag forces. These forces are lower in depressions  
623 where KF are more sheltered. This explanation must be advanced with caution,  
624 because the expected result involving the topography was a greater occurrence of  
625 KF on crests rather than depressions (S. Derrien, *com.pers.*). Indeed, global  
626 topography as used in this study is not efficient enough to predict KF variability

627 correctly in shallow water which leads to limited prediction between LAT and  $H_1$ . The  
628 BPI computed on a finer scale than the one used here at a 150m resolution, was  
629 expected to be a more reliable variable to explain KF distribution at shallower depths.  
630 The availability of proper high resolution depth data over the entire extent of the  
631 coast of Brittany remains a major issue. This leads us to data quality issues.

632

### 633 *Data quality – limitations and scale problem*

634 The digital echo sounding system successfully characterised KF in the surveyed  
635 areas and again demonstrated its ability to characterise and map aquatic vegetation,  
636 as shown and validated in previous studies (McRea et al. 1999; Piazzini et al. 2000;  
637 Brown et al. 2002; Freitas et al. 2003; Riegl et al. 2005; Freitas et al. 2006).

638 Nevertheless, the acoustic detection showed some limitations. The first one is the  
639 binary classification of substratum: rock or not. Since the survey was conducted with  
640 quite a small vessel, the results are sensitive to weather conditions and it is  
641 recommended that surveys be conducted under calm weather conditions (without  
642 swell and wind). Typical problems include: false KF detection, inaccuracy in the  
643 evaluation of the instantaneous depth and number of *Bottom Errors* increasing with  
644 wave height, leading to a degraded acoustic dataset. Research is still under way and  
645 better results are expected with the improvement of the clustering algorithm,  
646 particularly on some critical points:

- 647 - A decrease in the number of *Bottom Errors*. This would reduce the number of  
648 misdetection of KF, especially on rocky substrata.
- 649 - A better submerged aquatic vegetation classification. For this study, transects  
650 were mainly assessed in pure KF areas, but in some locations (particularly in  
651 very shallow waters), different submerged aquatic vegetation species could be

652 present (*Zostera marina* on the AW site, for example) and influence the  
653 classifying procedure. Better knowledge of the different species spectral  
654 signatures and taking them into account in the algorithm would reduce KF  
655 false detection.

656

657 Another type of input data required with the highest possible quality is the substratum  
658 layer. KF are predicted only where a rocky substrate is present, by way of a mask of  
659 the rocky area. At the working scale, i.e., pixels of 150 m covering the entire coast of  
660 Brittany, these prediction errors are without consequences, since the obtained map  
661 provides the prediction of the distribution and the inter-site variation of KF  
662 frequencies at a global scale. However, if this model was adapted to finer scales in  
663 order to predict local distributions and intra-site variations of KF, the current scale of  
664 the substratum layer (not better than 1:500,000) would not be efficient and would  
665 have to be refined. High resolution Lidar data, for example, could overcome this  
666 limitation at a local scale. The ability of Lidar data to finely characterise seabed  
667 substratum types was tested in recent studies (Rosso et al. 2006; Méléder et al. 2007).  
668 Its high vertical and horizontal accuracy make it suitable to map bottom roughness and  
669 topography in great detail (although at a high cost!).

670 Obviously, a good balance should be sought in scale homogeneity between source  
671 data. For example, distribution laws as a function of depth used for model calibration  
672 and validation were established using field bathymetry data from echo soundings,  
673 whereas the model input raster dataset used for prediction was generated from  
674 various sources at various resolutions (a mix of Lidar, digital soundings and map  
675 soundings). Depth values from these two sources (map vs. field) exhibit  
676 discrepancies leading to misprediction. For example, KF could be predicted on the

677 map for an area where field depths were too great to be photosynthetically efficient or  
678 conversely, some map areas where no KF were predicted corresponded to small  
679 field depths allowing KF growth.

680 At the end of day, satellite data from SeaWiFS and AVHRR used are in accordance  
681 with the current working scale for prediction at regional scale. However, similarly to  
682 the substratum and bathymetry issues, image resolution limits the use of the model  
683 for prediction at a local scale. MERIS, an ocean colour sensor aboard the Envisat  
684 satellite, with a pixel resolution of 300 m, will also allow progress towards finer  
685 scales.

686 While progress is expected from regional to local levels, additional parameters may  
687 have to be introduced in the model, as they may have an effect on KF at local scale,  
688 and this would require new investigations. For example, the effect of faunal  
689 abundance consuming primary producers or the swell effect through drag forces  
690 and/or abrasion of rocky area by sand, fine topography, must be tested.

691

## 692 CONCLUSION

693 The proposed model enabled the prediction of KF frequency over time and space as  
694 a function of water transparency and exposure, at a global scale that is effective in  
695 the context of Climate Change. Its main limits were: a) predictions in shallow water  
696 where the bathymetry at the working scale was not fine enough and b) the mostly  
697 coarse scale of source data which did not allow local effects to be assessed. These  
698 two limits could be overcome with an adaptation of the model, including refinement of  
699 the working source data and the addition of new key parameters influencing  
700 communities at local scales. Nevertheless, the current model is a good decisional  
701 tool at a global scale, as in the context of Climate Change, allowing us to predict

702 changes in the KF depth limit which could be used as an indicator of the health of  
703 these communities and those associated with them.

704

705

706

707

708

709

710 REFERENCES

- 711 Bajjouk T, Guillaumont B, Populus J (1996) Application of airborne imaging  
712 spectrometry system data to intertidal seaweed classification and mapping.  
713 HYDROBIOLOGIA 327: 463-471
- 714 Belsher T (1986) Etude bibliographique de quelques espèces planctoniques et  
715 benthiques de la Manche. Vol. 4 : Phytobenthos. Ifremer, Brest
- 716 Boller ML, Carrington E (2006) The hydrodynamic effects of shape and size change  
717 during reconfiguration of a flexible macroalga. J EXP BIOL 209: 1894-1903
- 718 Brinkman AG, Dankers N, van Stralen M (2002) An analysis of mussel bed habitats  
719 in the Dutch Wadden Sea. HELGOLAND MAR RES 56: 59-75
- 720 Brown CJ, Cooper KM, Meadows WJ, Limpenny DS, Rees HL (2002) Small-scale  
721 mapping of sea-bed assemblages in the eastern English Channel using  
722 sidescan sonar and remote sampling techniques. ESTUAR COAST SHELF S  
723 54: 263-278
- 724 Buck BH, Buchholz CM (2005) Response of offshore cultivated *Laminaria saccharina*  
725 to hydrodynamic forcing in the North Sea. AQUACULTURE 250: 674-691
- 726 Cardoso PG, Raffaelli D, Lillebø AI, Verdelhos T, Pardal MA (2008) The impact of  
727 extreme flooding events and anthropogenic stressors on macrobenthic  
728 communities' dynamics. ESTUAR COAST SHELF S 76: 553-565
- 729 Combe JP, Launeau P, Carrere V, Despan D, Meleder V, Barille L, Sotin C (2005)  
730 Mapping microphytobenthos biomass by non-linear inversion of visible-  
731 infrared hyperspectral images. REMOTE SENS ENVIRON 98: 371-387
- 732 Dayton PK, Tegner MJ, Parnell PE, Edwards PB (1992) Temporal and spatial  
733 patterns of disturbance and recovery in a kelp forest community. ECOL  
734 MONOGR 62: 421-445
- 735 de Jonge VN, de Jong DJ (2002) 'Global Change' impact of inter-annual variation in  
736 water discharge as a driving factor of dredging and spoil disposal in the river  
737 Rhine system and of turbidity in the Wadden sea. ESTUAR COAST SHELF S  
738 55: 969-991
- 739 De Oliveira E, Populus J, Guillaumont B (2006) Predictive modelling of coastal  
740 habitats using remote sensing data and fuzzy logic. EARSeL eProceedings 5:  
741 208-223
- 742 Denny M (1995) Predicting physical disturbance: mechanistic approaches to the  
743 study of survivorship on wave-swept shores. ECOL MONOGR 65: 371-418
- 744 Denny M, Gaylord B (2002) The mechanics of wave-swept algae. J EXP BIOL 205:  
745 1355-1362
- 746 Ferrat L, Pergent-Martini C, Roméo M (2003) Assessment of the use of biomarkers in  
747 aquatic plants for the evaluation of environmental quality: application to  
748 seagrasses. AQUAT TOXICOL 65: 187-204
- 749 Freitas R, Rodrigues AM, Quintino V (2003) Benthic biotopes remote sensing using  
750 acoustics. J EXP MAR BIOL ECOL 285-286: 339-353
- 751 Freitas R, Sampaio L, J. O, Rodrigues AM, Quintino V (2006) Validation of soft  
752 bottom benthic habitats identified by single-beam acoustics. MAR POLLUT  
753 BULL 53: 72-79
- 754 Gaylord B, Denny M, Koehl MAR (2003) Modulation of wave forces on kelp canopies  
755 by alongshore currents. LIMNOL OCEANOGR 48: 860-871
- 756 Gohin F, Loyer S, Lunven M, Labry C, Froidefond J-M, Delmas D, Huret M, Herbland  
757 A (2005) Satellite-derived parameters for biological modelling in coastal

758 waters: Illustration over the eastern continental shelf of the Bay of Biscay.  
759 REMOTE SENS ENVIRON 95: 29-46

760 Greve TM, Krause-Jensen D (2005) Predictive modelling of eelgrass (*Zostera*  
761 marina) depth limits. MAR BIOL 146: 849-858

762 Guillaumont B, Bajjouk T, Talec P (1997) Seaweed and remote sensing: a critical  
763 review of sensors and data processing. In: Round FE, Chapman DJ (eds)  
764 Progress in Phycological Research. Biopress, pp 213-282

765 Guillaumont B, Callens L, Dion P (1993) Spatial-Distribution and Quantification of  
766 Fucus Species and Ascophyllum-Nodosum Beds in Intertidal Zones Using  
767 Spot Imagery. HYDROBIOLOGIA 261: 297-305

768 Hurd CL (2000) Water motion, marine macroalgae, physiology, and production. J  
769 PHYCOL 36: 453-472

770 IPCC (2001) Climate change 2001: the scientific basis, contribution of working group  
771 I to the third assessment report of the Intergovernmental Panel on Climate  
772 Change (IPCC). Cambridge University Press, Cambridge

773 Kelly NM, Fonseca M, Whitfield P (2001) Predictive mapping for management and  
774 conservation of seagrass beds in North Carolina. AQUAT CONSERV 11: 437-  
775 451

776 Koutsikopoulos C, Beillois P, Leroy C, Taillefer F (1998) Temporal trends and spatial  
777 structures of the sea surface temperature in the Bay of Biscay. OCEANOL  
778 ACTA 21: 335-344

779 Lundblad ER, Wright DJ, Naar DF, Donahue BT, Miller J, Larkin EM, Rinehart R  
780 (2004) Classifying deep water benthic habitats around Tutulia, America  
781 Samoa 24th annual ESRI Conference, San Diego, CA

782 Marchalot C, Diner N, Berger L (2003) MOVIES+ documentation: Echo-integration by  
783 depth layers using MOVIES+ software. IFREMER/DNIS/ESI, Plouzané

784 Markager S, Sand-Jensen K (1992) Light requirements and depth zonation of marine  
785 macroalgae. MAR ECOL-PROG SER 88: 83-92

786 McRea JE, Greene HG, O'Connell VM, Wakefield WW (1999) Mapping marine  
787 habitats with high resolution sidescan sonar. OCEANOL ACTA 22: 679-686

788 MEDD (2005) Plan d'actions stratégique du MEDD pour les milieux marins. Tome 1 -  
789 Diagnostic et Orientations. Ministère de l'écologie et du développement  
790 durable, Paris

791 Méléder V, Launeau P, Barillé L, Rincé Y (2003) Microphytobenthos assemblage  
792 mapping by spatial visible-infrared remote sensing in a shellfish ecosystem. C  
793 R BIOL 11: 437-451

794 Méléder V, Populus J, Rollet C (2007) Mapping seabed substrata using Lidar remote  
795 sensing. MESH - Mapping European Seabed Habitats.  
796 [http://www.searchmesh.net/PDF/GMHM3\\_Mapping\\_Substrata\\_using\\_LIDAR.](http://www.searchmesh.net/PDF/GMHM3_Mapping_Substrata_using_LIDAR.pdf)  
797 [pdf](http://www.searchmesh.net/PDF/GMHM3_Mapping_Substrata_using_LIDAR.pdf)

798 Ménesguen A, Piriou JY, Dion P, Auby I (1997) Les "Marées vertes", un exemple  
799 d'eutrophisation à macroalgues. In: Dauvin J-C (ed) Les biocénoses marines  
800 et littorales françaises des côtes atlantiques, Manche et Mer du Nord.  
801 Synthèse, menaces et perspectives. MNHN, Paris, pp 212-218

802 Norderhaug KM, Christie H, Rinde E (2002) Colonisation of kelp imitations by  
803 epiphyte and holdfast fauna; a study of mobility patterns. MAR BIOL 141: 965-  
804 973

805 Piazzzi L, Acunto S, Cinelli F (2000) Mapping of *Posidonia oceanica* beds around Elba  
806 Island (western Mediterranean) with integration of direct and indirect methods.  
807 OCEANOL ACTA 23: 339-346

808 Pope ND, Widdows J, Brinsley MD (2006) Estimation of bed shear stress using the  
809 turbulent kinetic energy approach. A comparison of annular flume and field  
810 data. CONT SHELF RES 26: 959-970  
811 Riegl BM, Moyer RP, Morris LJ, Virnstein RW, Purkis SJ (2005) Distribution and  
812 seasonal biomass of drift macroalgae in the Indian River Lagoon (Florida,  
813 USA) estimated with acoustic seafloor classification (QTCView, *Echoplus*). J  
814 EXP MAR BIOL ECOL 326: 89-104  
815 Roff JC, Taylor ME (2000) National frameworks for marine conservation - A  
816 hierarchical geophysical approach. AQUAT CONSERV 10: 209-223  
817 Rosso PH, Ustin SL, Hastings A (2006) Use of lidar changes associated with  
818 *Spartina* invasion in San Francisco Bay marshes. REMOTE SENS ENVIRON  
819 100: 295-306  
820 SHOM (1994-2005) Cartes sédimentologiques (G). SHOM  
821 Sivertsen K (1997) Geographic and environmental factors affecting the distribution of  
822 kelp beds and barren grounds and changes in biota associated with kelp  
823 reduction at sites along the Norwegian coast. CAN J FISH AQUAT SCI 54:  
824 2872-2887  
825 Stevens T, Connolly RM (2004) Testing the utility of abiotic surrogates for marine  
826 habitat mapping at scales relevant to management. BIOL CONSERV 119:  
827 351-362  
828 Toms JD, Lesperance ML (2003) Piecewise regression: A tool for identifying  
829 ecological thresholds. ECOLOGY 84: 2034-2041  
830 Vaslet D, Larsonneur C, Auffret J-P (1979) Carte des sédiments superficiels de la  
831 Manche. BRGM/CNEXO  
832 Vogel S (1994) Life in Moving Fluids (2nd edn). Princeton University Press,  
833 Princeton, pp 467 pp.  
834 Zacharias MA, Morris MC, Howes DE (1999) Large scale characterization of intertidal  
835 communities using a predictive model. J EXP MAR BIOL ECOL 239: 223-242  
836 Zacharias MA, Roff JC (2001) Explanations of patterns of intertidal diversity at  
837 regional scales. J BIOGEOGR 28: 471-483  
838  
839

840 Figure legend

841

842 Figure 1. Location of the 10 sites. Black star: sites used to build the model; white  
843 star: sites used to validate it.

844

845 Figure 2. Echo-integration by depth layers in dense kelp forest (KF) on a selected  
846 part of the acoustic transect. A: bottom line – Seafloor; B: offset line – down limit of  
847 the Kelp forest integrated layer (0.2 meters above bottom); C: Top limit of the  
848 integrated layer (2.2 meters above bottom). The vertical lines delimit each ESU (20  
849 ping width).

850

851 Figure 3. Kelp forest frequency vs. depth. Example from the site Molène, Mo (cf.  
852 Figure 1). Observations (O) are obtained from echo-sounding and are fitted using  
853 piecewise regression (bold line), fixing the two breakpoints,  $H_1$  and  $H_2$ , and the slope  
854 between these points,  $Slope_2$ . Fit is expressed with its prediction (fine line) and  
855 confidence (dashed line) intervals at 95 %.

856

857 Figure 4. Weekly water transparency, expressed in  $K_{PAR}$ , derived from SeaWiFS data  
858 averaged over the 1998-2004 period. a/ Sites used for model building; b/ Sites used  
859 for model validation.

860

861 Figure 5. Weekly temperature, expressed in SST, derived from AVHRR data  
862 averaged over the two past decades. a/ Sites used for model building; b/ Sites used  
863 for model validation.

864

865 Figure 6. Example of an echogram along a selected acoustic transect (from GI site,  
866 cf. Figure 1). The results of the cluster analysis classification procedure of KF  
867 presence (LAMINAIRE) or absence (empty box) are presented in table above  
868 echogram with the corresponding bathymetry (m). For *BOTT-ERR* definition, see  
869 Materials and Methods section.

870

871 Figure 7. KF frequency observed vs. predicted with the four significant models for  
872 depth ranging from  $H_1$  to  $H_2$  at the five sites used to build model: AW, Mo, Me, Tr  
873 and Gr. a/ pred\_mod1: model using SSTmin only (eqs. 11 to 13), b/ pred\_mod2:  
874 model using  $K_{PARmin}$  (eqs. 14 to 16), c/ pred\_mod3: model using  $K_{PARmin}$  and  
875  $V_{max}^{1.5}$  (eqs. 14, 16 and 17), d/ pred\_mod4: model using SSTmin and  $V_{max}^{1.5}$  (eqs.  
876 11, 13 and 18). Dark lines illustrate the relationship observation = prediction.

877

878 Figure 8. KF frequency observed vs. predicted using BPI (eq. 9), for depth less than  
879  $H_1$  at the five sites used to build model: AW, Mo, Me, Tr and Gr. Dark lines illustrate  
880 the relationship observation = prediction.

881

882 Figure 9. Model validation. KF frequency observed vs. predicted at the five sites  
883 used to valid model: Au, Br, GI, He, MI. a/ prediction for depth ranging from  $H_1$  to  $H_2$   
884 using  $K_{PARmin}$  and  $V_{max}^{1.5}$  (pred\_mod3; eqs. 14, 16 and 17), or SSTmin and  
885  $V_{max}^{1.5}$  (pred\_mod4; eqs. 11, 13 and 18) when no turbidity data are available; b/  
886 prediction for depth less than  $H_1$  using BPI (eq. 19).

887

888 Figure 10. Predictive map of KF presence percentage. Three zooms are shown to  
889 illustrate results: AW, Br and GI, respectively in black, red and blue boxes.

890

891

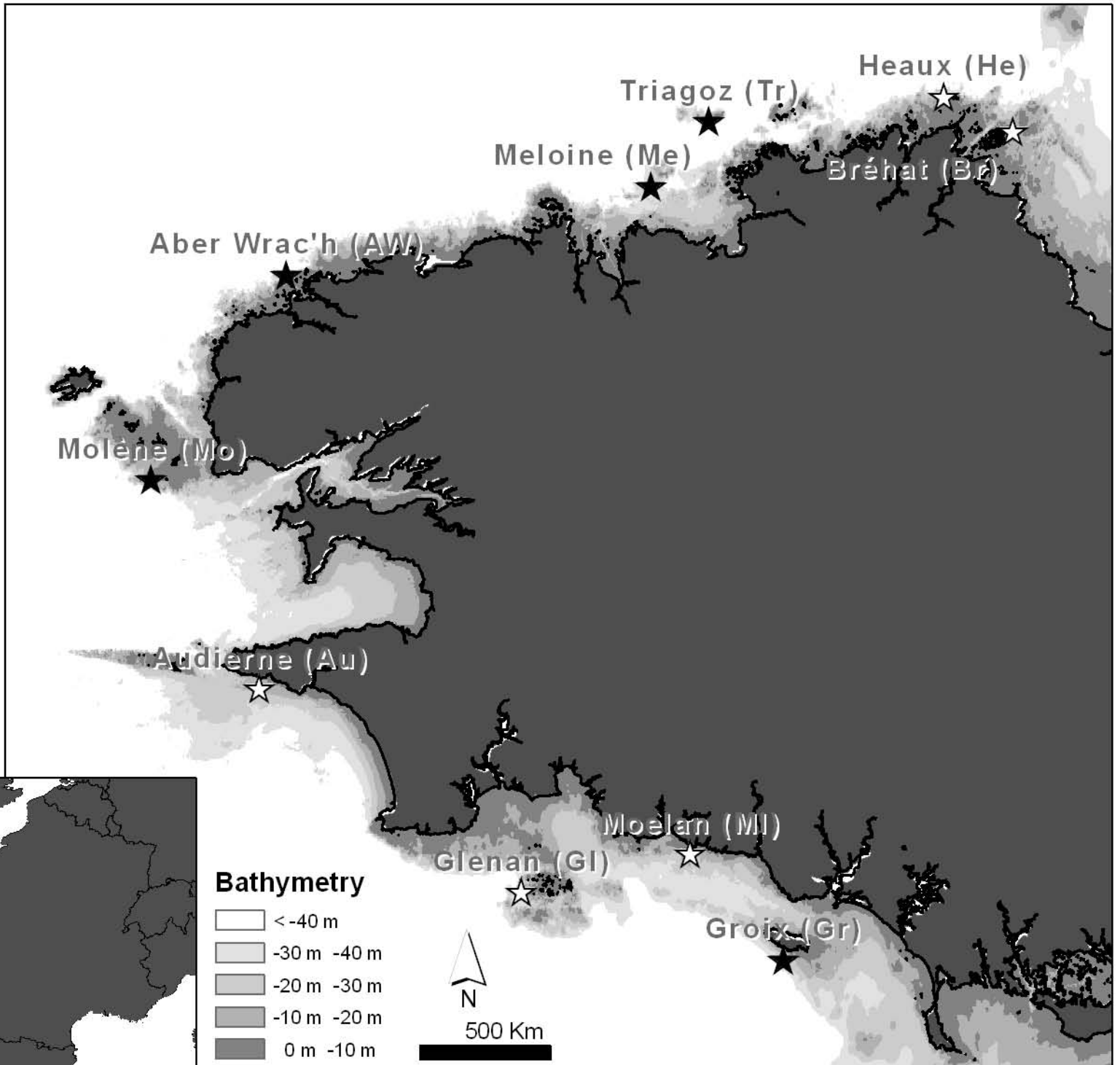
892

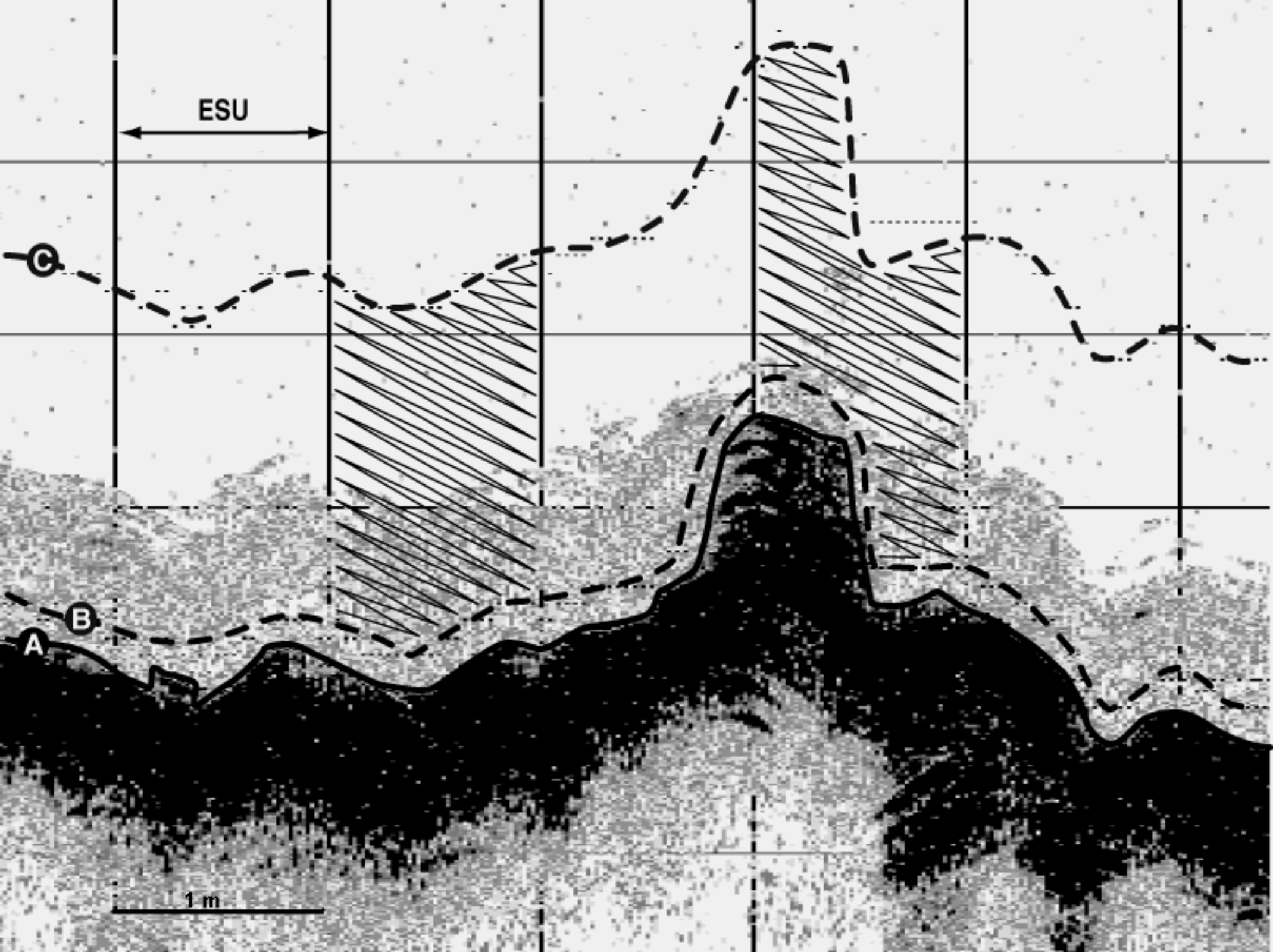
893

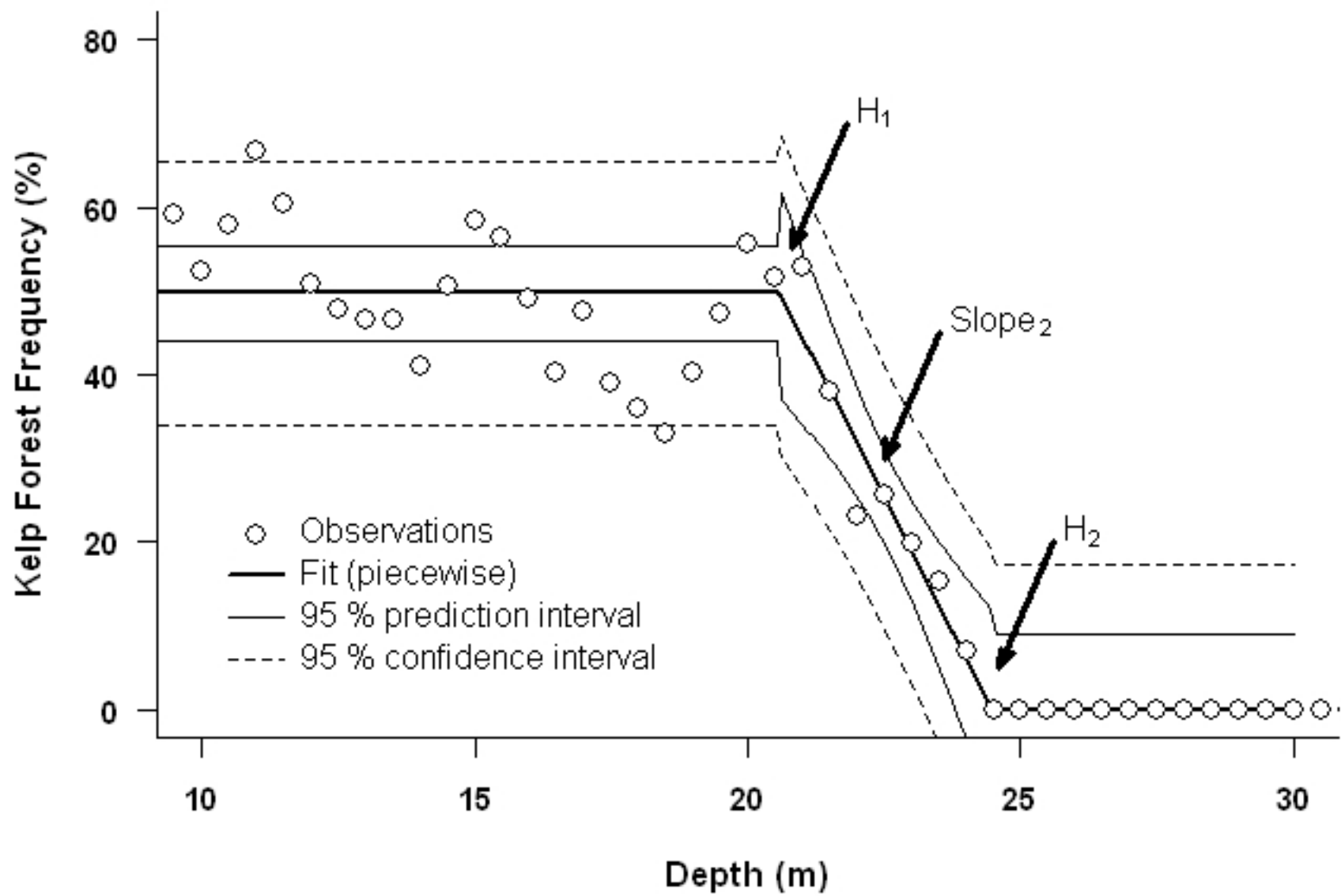
894

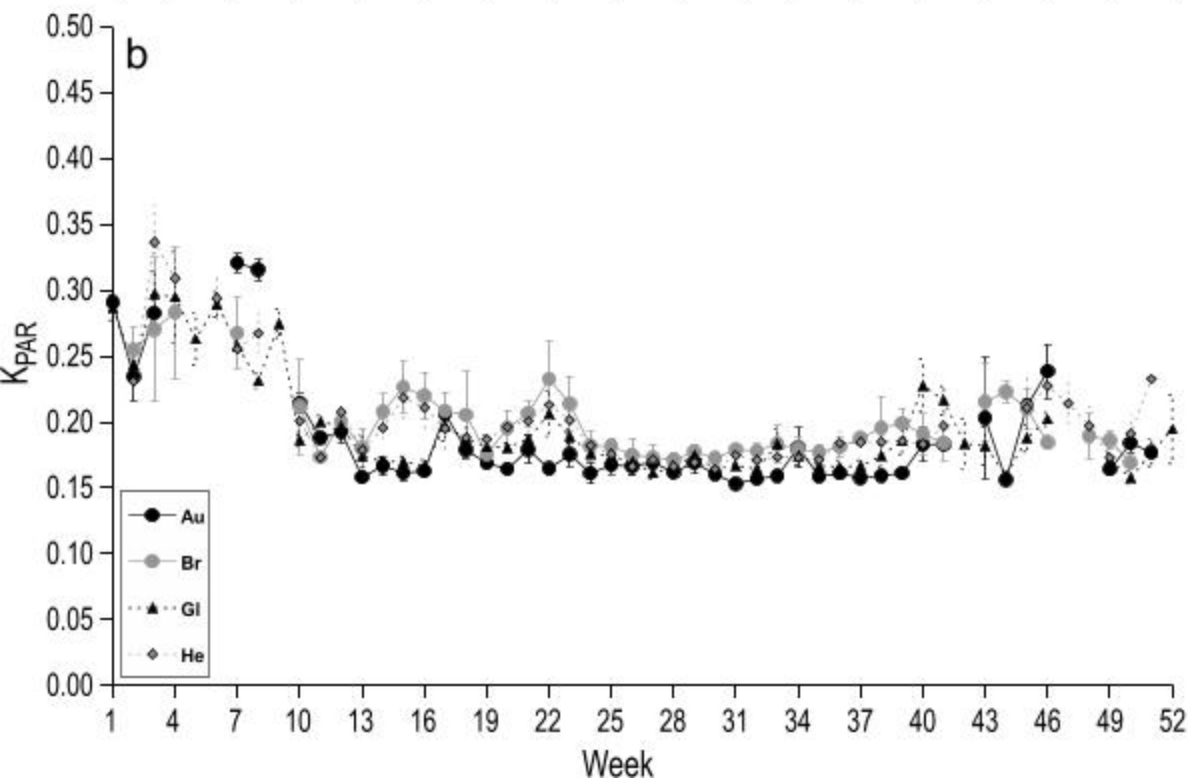
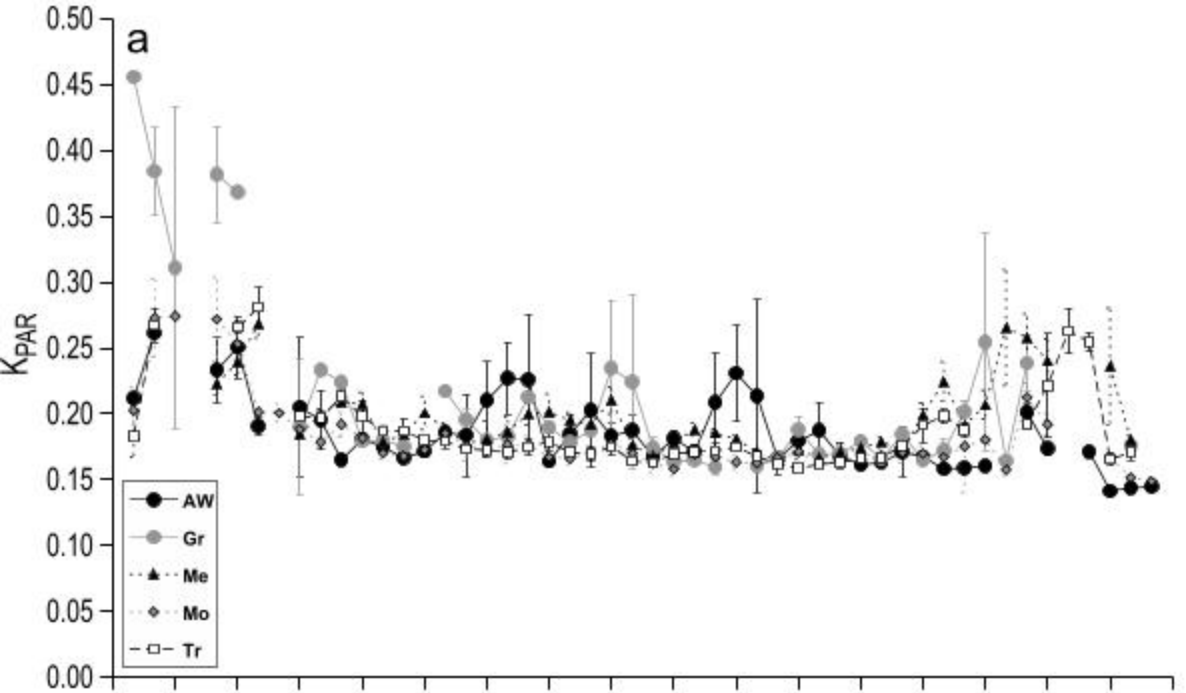
895

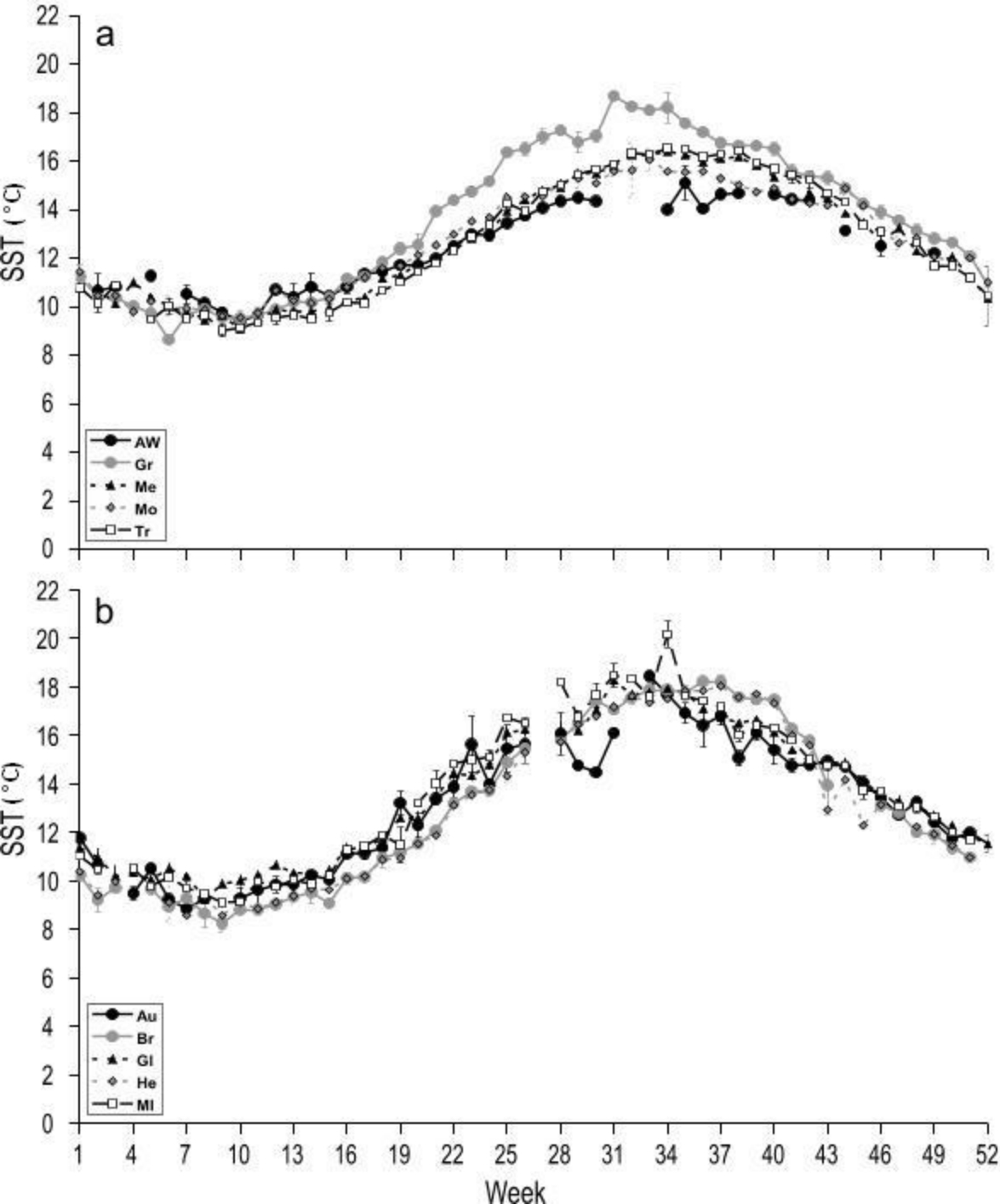
896





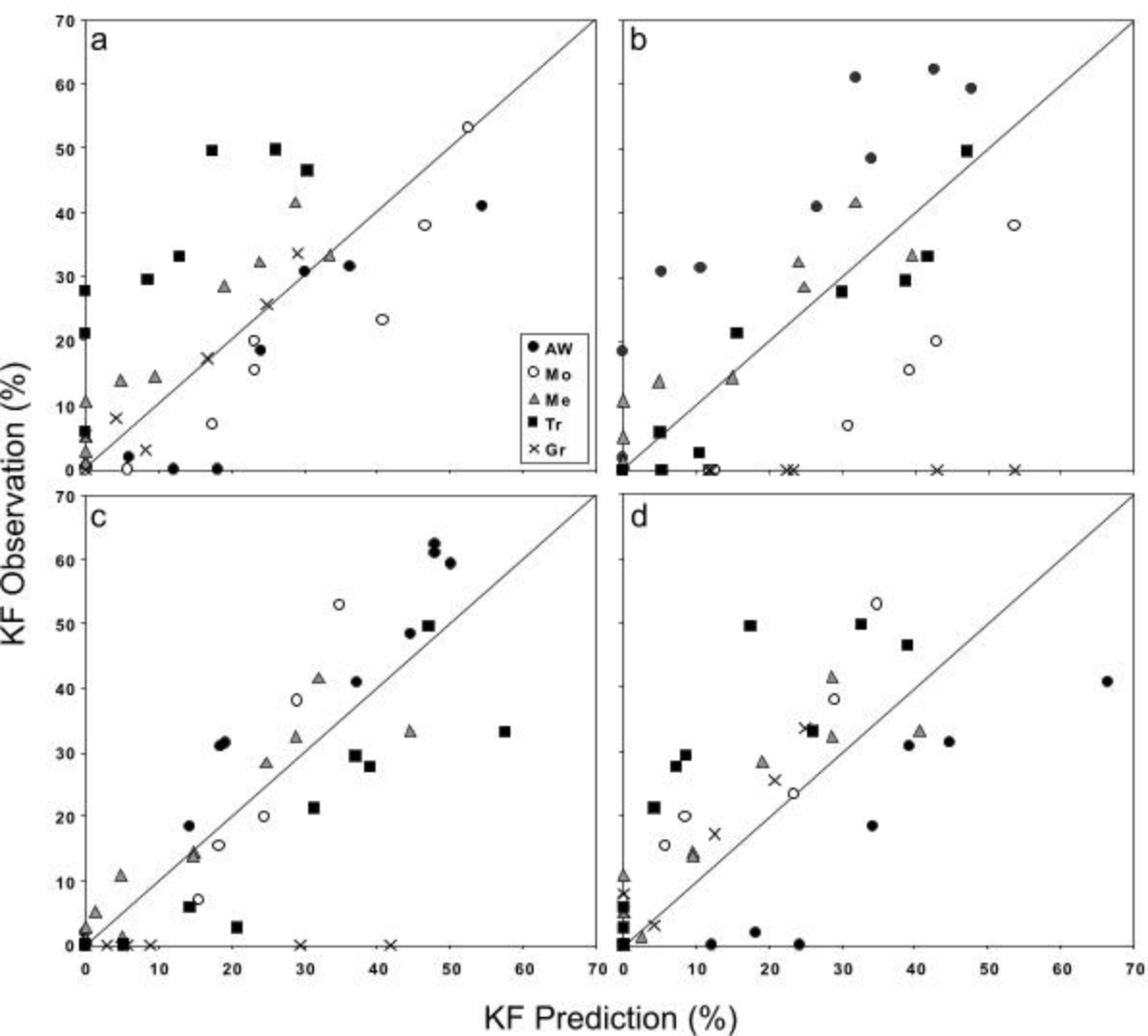




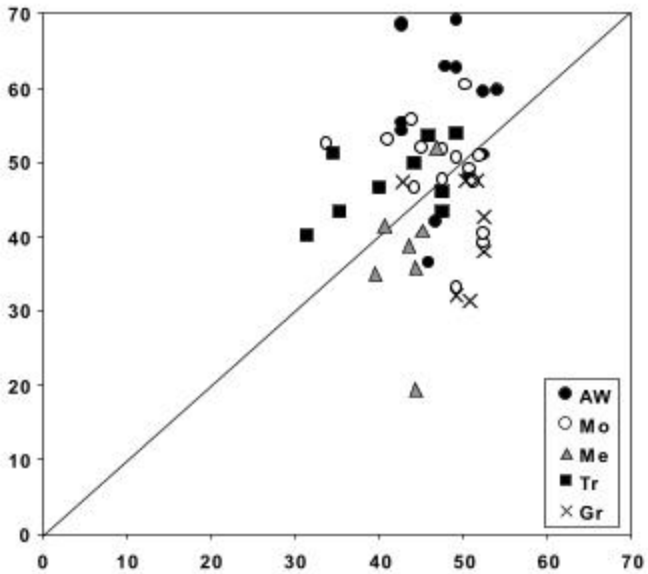


5 m

TPS	Z corr	Classif 2
12:58:48	9,63	LAMINAIRE
12:58:49	10,13	LAMINAIRE
12:58:50	10,03	
12:58:51	10,33	<i>BOTT-ERR</i>
12:58:52	10,33	
12:58:52	10,23	<i>BOTT-ERR</i>
12:58:53	10,13	<i>BOTT-ERR</i>
12:58:54	9,53	<i>BOTT-ERR</i>
12:58:55	9,63	LAMINAIRE
12:58:56	10,23	LAMINAIRE
12:58:56	10,53	LAMINAIRE
12:58:57	10,83	LAMINAIRE
12:58:58	11,03	LAMINAIRE
12:58:59	11,23	LAMINAIRE
12:59:00	11,03	
12:59:01	11,13	LAMINAIRE
12:59:01	11,63	
12:59:02	11,33	<i>BOTT-ERR</i>
12:59:03	12,03	<i>BOTT-ERR</i>
12:59:04	11,33	<i>BOTT-ERR</i>
12:59:05	11,73	
12:59:06	12,43	<i>BOTT-ERR</i>
12:59:07	12,23	LAMINAIRE
12:59:08	12,33	LAMINAIRE
12:59:08	12,73	
12:59:09	12,93	
12:59:10	13,24	<i>BOTT-ERR</i>
12:59:11	12,74	LAMINAIRE
12:59:12	12,84	
12:59:13	13,14	
12:59:14	13,04	
12:59:15	12,94	
12:59:16	12,84	LAMINAIRE
12:59:17	12,54	LAMINAIRE
12:59:18	12,24	LAMINAIRE
12:59:19	12,74	<i>BOTT-ERR</i>
12:59:20	12,34	
12:59:21	13,04	LAMINAIRE
12:59:21	12,94	LAMINAIRE
12:59:22	12,84	LAMINAIRE
12:59:23	13,14	LAMINAIRE
12:59:24	13,04	
12:59:25	12,84	LAMINAIRE
12:59:26	12,84	LAMINAIRE
12:59:27	12,94	LAMINAIRE
12:59:28	12,44	LAMINAIRE
12:59:29	12,54	LAMINAIRE
12:59:30	12,64	LAMINAIRE
12:59:31	11,94	LAMINAIRE
12:59:32	11,64	LAMINAIRE
12:59:33	11,34	LAMINAIRE

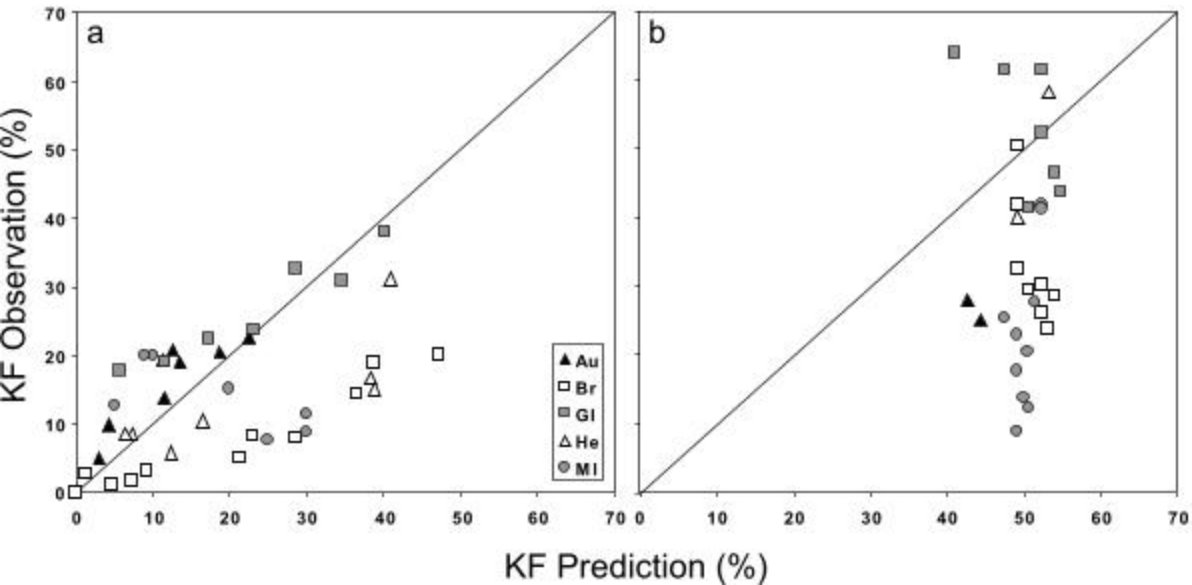


KF Observation (%)



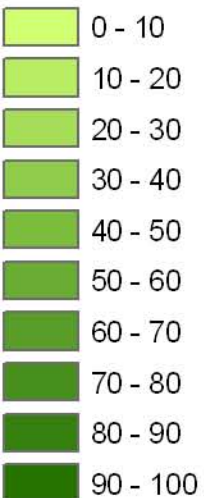
KF Prediction (%)

- AW
- Mo
- △ Me
- Tr
- × Gr

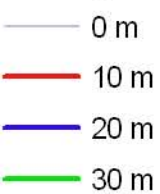


### KF presence percentage

rock without KF



### isoheight



### Substratum nature

rocky area

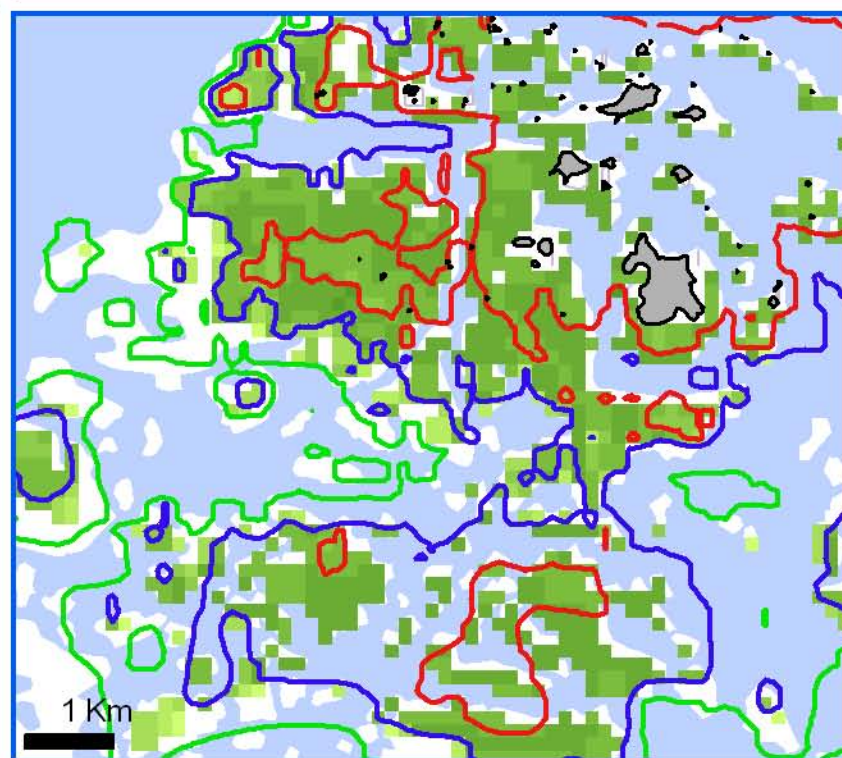
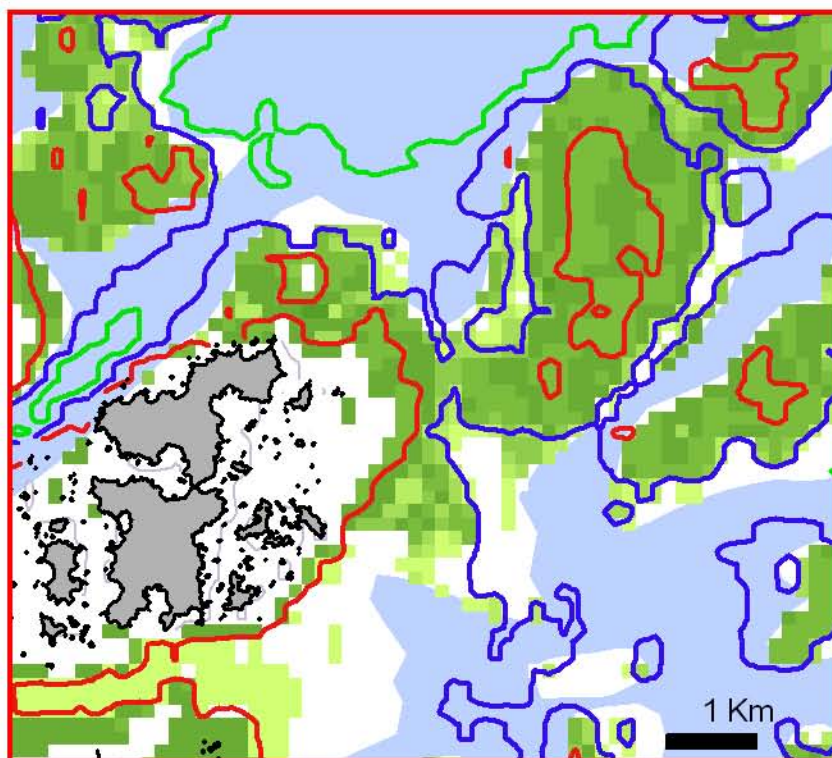
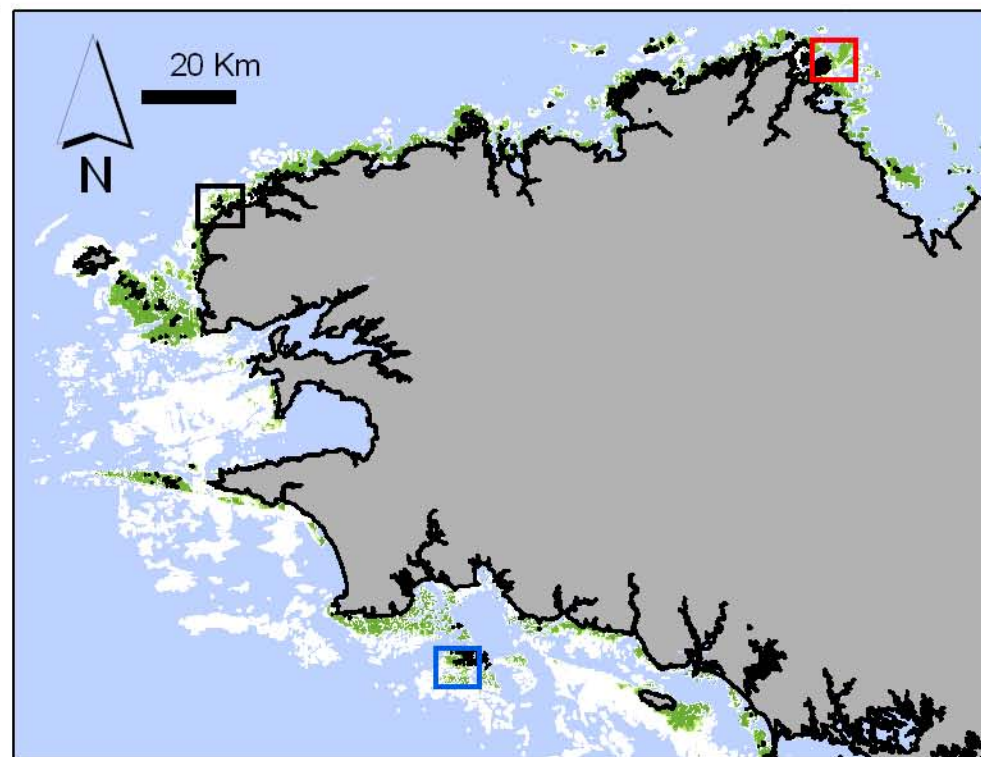
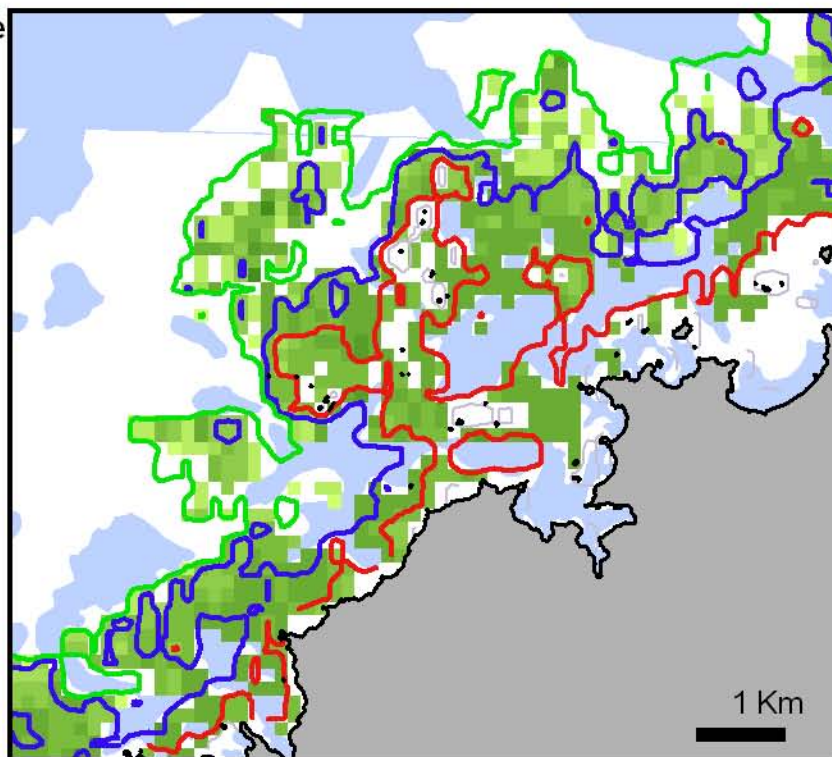


Table 1. Environmental parameters used in stepwise regression processes. Training sites are underlined, the others are validation sites.

	$K_{PARyear}$	$K_{PARgrowth}$	$K_{PARmin}$	$K_{PARmax}$	SSTyear	SSTgrowth	SSTmin	SSTmax	Vmax
<u>AW</u>	0.201	0.190	0.175	0.261	12.4	11.9	9.4	15.1	1.12
<u>Gr</u>	0.265	0.194	0.202	0.456	13.6	12.9	8.7	18.7	0.27
<u>Me</u>	0.215	0.191	0.183	0.268	12.7	11.6	9.1	16.4	0.89
<u>Mo</u>	0.197	0.173	0.160	0.274	12.8	12.1	9.6	16.1	0.27
<u>Tr</u>	0.202	0.176	0.176	0.281	12.7	11.5	9.0	16.5	0.95
Au	0.205	0.171	0.164	0.321	13.1	12.7	8.9	18.5	0.44
Br	0.220	0.205	0.189	0.283	13.0	11.7	8.3	18.2	0.87
Gl	0.218	0.182	0.164	0.297	13.5	12.8	9.3	18.3	0.27
He	0.222	0.197	0.182	0.337	13.0	11.6	8.6	18.0	0.87
MI	-	-	-	-	13.7	12.9	9.1	20.2	0.1

Table 2. Breakpoints  $H_1$  and  $H_2$  and the slope between them,  $Slope_2$ , fitted using piecewise regressions. All regressions and fit parameters are significant ( $p \leq 0.01$ ) except for sites Au, He and MI (n.s: not significant). Training sites are underlined, the others are validation sites.

	<u>AW</u>	<u>Gr</u>	<u>Me</u>	<u>Mo</u>	<u>Tr</u>	Au	Br	Gl	He	MI
adjusted $R^2$	0.92	0.96	0.88	0.90	0.96	0.80	0.92	0.98	0.98	0.97
$H_1 \pm \text{std}$	$19.9 \pm 0.4$	$15.5 \pm 0.4$	$19.3 \pm 0.6$	$20.6 \pm 0.5$	$18.8 \pm 0.4$	n.s.	$13.2 \pm 0.6$	$15.2 \pm 0.3$	$15.5 \pm 0.1$	n.s.
$Slope_2 \pm \text{std}$	$-11.5 \pm 1.5$	$-8.9 \pm 0.8$	$-8.8 \pm 0.9$	$-12.5 \pm 0.8$	$-9.3 \pm 1.1$	$-3.6 \pm 0.4$	$-4.9 \pm 0.4$	$-6.0 \pm 0.2$	n.s.	n.s.
$H_2 \pm \text{std}$	$25.2 \pm 0.5$	$19.6 \pm 0.4$	$23.4 \pm 0.6$	$24.5 \pm 0.6$	$23.8 \pm 0.4$	$22.3 \pm 1.6$	$21.7 \pm 0.8$	$25.8 \pm 0.4$	$27.8 \pm 1.4$	$22.3 \pm 0.8$

Table 3. Fraction of incident light (in %),  $Fr$ , reaching KF depth limit  $H_2$ .  $Fr$  values are calculated (eq. 1) for four water transparency variables:  $K_{PARyear}$ ,  $K_{PARgrowth}$ ,  $K_{PARmin}$  and  $K_{PARmax}$ .  $Fr$  is not estimated for the site MI, because no turbidity data are available. Training sites are underlined, the others are validation sites.

	$Fr_{H_2} (K_{PARyear})$	$Fr_{H_2} (K_{PARgrowth})$	$Fr_{H_2} (K_{PARmin})$	$Fr_{H_2} (K_{PARmax})$
<u>AW</u>	0.66	0.80	1.26	0.15
<u>Gr</u>	0.57	2.32	1.95	0.62
<u>Me</u>	0.64	1.17	1.36	0.18
<u>Mo</u>	0.80	1.41	1.98	0.12
<u>Tr</u>	0.78	1.51	1.46	0.12
Au	1.04	2.19	2.56	0.08
Br	0.84	1.17	1.65	0.21
Gl	0.36	0.91	1.44	0.05
He	0.21	0.42	0.63	0.01
MI	-	-	-	-

Table 4. Prediction of KF depth limit H<sub>2</sub>. Observed H<sub>2</sub> are from piecewise regression (Table 2), predicted and simulated H<sub>2</sub> are from predictive model (pred\_mod3 or pred\_mod4\*) but simulated ones follow varied scenarios (see text for detail). Training sites are underlined, the others are validation sites.

Site	Observed H <sub>2</sub>	Predicted H <sub>2</sub>	Simulated H <sub>2(0.01)</sub>	Simulated H <sub>2(0.02)</sub>	Simulated H <sub>2(0.05)</sub>
<u>AW</u>	25.2 ± 0.5	25.0 ± 0.6	23.8 ± 0.6	22.4 ± 0.6	19.0 ± 0.6
<u>Gr*</u>	19.6 ± 0.4	20.2 ± 0.0	21.2 ± 0.4	22.8 ± 0.4	25.5 ± 0.4
<u>Me</u>	23.4 ± 0.6	23.3 ± 0.4	22.1 ± 0.4	20.8 ± 0.4	17.2 ± 0.4
<u>Mo</u>	24.5 ± 0.6	24.3 ± 0.5	23.3 ± 0.5	22.0 ± 0.5	18.4 ± 0.5
<u>Tr</u>	23.8 ± 0.4	24.3 ± 0.8	23.1 ± 0.8	21.9 ± 0.8	18.2 ± 0.8
Au*	22.3 ± 1.6	20.3 ± 0.1	21.4 ± 0.1	23.0 ± 0.1	25.7 ± 0.1
Br	21.7 ± 0.8	22.5 ± 0.5	21.26 ± 0.5	20.0 ± 0.5	16.4 ± 0.5
Gl	25.8 ± 0.4	24.0 ± 0.1	22.8 ± 0.1	21.6 ± 0.1	17.9 ± 0.1
He	27.8 ± 1.4	23.3 ± 1.6	22.1 ± 1.6	20.9 ± 1.6	17.3 ± 1.6
MI*	22.3 ± 0.8	21.8 ± 0.0	23.0 ± 0.0	24.6 ± 0.0	27.2 ± 0.0